RESEARCH ARTICLE SUMMARY

STRUCTURAL BIOLOGY
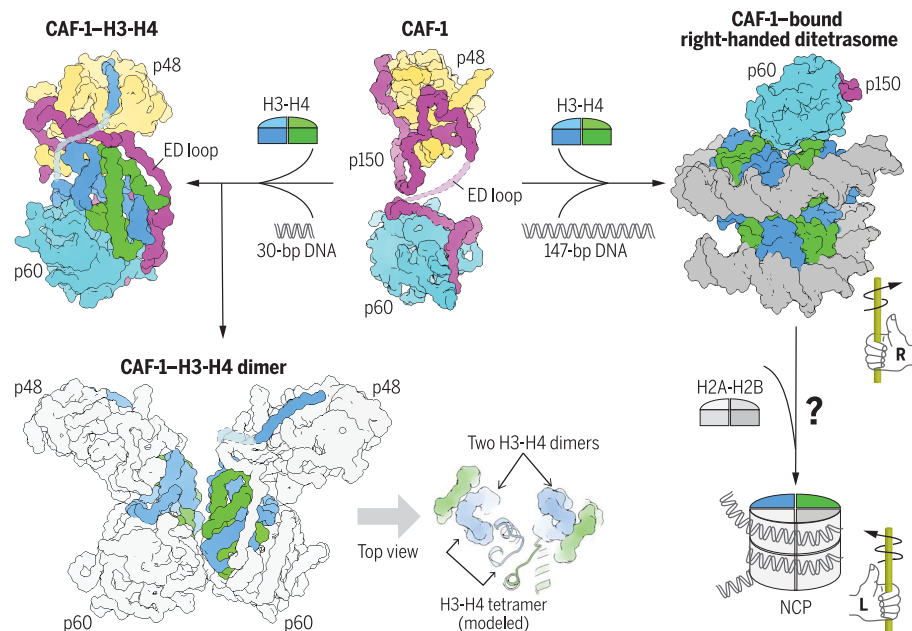
Structural insights into histone binding and nucleosome assembly by chromatin assembly factor-1

Chao-Pei Liu*†, Zhenyu Yu†, Jun Xiong†, Jie Hu†, Aoqun Song†, Dongbo Ding†, Cong Yu, Na Yang, Mingzhu Wang, Juan Yu, Peini Hou, Kangning Zeng, Zhenyu Li, Zhuqiang Zhang, Xinzheng Zhang, Wei Li, Zhiguo Zhang, Bing Zhu*, Guohong Li*, Rui-Ming Xu*

INTRODUCTION: Inheritance of chromatin structure during cell division is essential for genome integrity and epigenetic inheritance. DNA replication disrupts parental nucleosomes, and nascent nucleosomes must be assembled on replicated DNA. Half of the histones for the replication-coupled nucleosome assembly are of parental origin, and the other half are newly synthesized. Chromatin assembly factor-1 (CAF-1) is an evolutionarily conserved heterotrimeric protein complex responsible for the deposition of newly synthesized histones H3 and H4 onto DNA. A mechanistic understanding of the structure and function of CAF-1 is needed to fully comprehend the principles of chromatin inheritance.

RATIONALE: We determined the crystal structure of the core domain of human CAF-1 in the absence of histones and used cryo–electron microscopy (cryo-EM) to solve the structure of CAF-1 bound to histones H3 and H4. Structural findings were corroborated with in vitro supercoiling assays and in vivo nascent nucleosome mapping analyses. We also investigated the handedness of the nucleosome precursor assembled by CAF-1 using a single-molecule freely orbiting magnetic tweezer (FOMT) method.

RESULTS: The crystal structure of the CAF-1 core domain shows that, in the absence of his-

tones, it adopts a bilobal structure, with the p48 and p60 subunits freely tethered by the middle domain of the p150 subunit. Upon the binding of an H3-H4 heterodimer, p48 and p60 hug the opposite ends of the elongated H3-H4 heterodimer, whereas the negatively charged ED loop of p150 secures the binding by traversing the hunched positively charged surface of the H3-H4 dimer. The C-terminal portion of the ED loop plays a particularly important role in CAF-1's histone binding and nucleosome assembly activities, as shown by in vitro histone binding and plasmid supercoiling assays, as well as in vivo nucleosome assembly analysis. The observed histone binding mode ensures that only one H3-H4 heterodimer is bound by a CAF-1 complex because the joining of a second H3-H4 dimer in the manner of a H3-H4 tetramer would be sterically prohibited by p60, which suggests that formation of an H3-H4 tetramer is regulated. A p60 cancer mutation located at the interface with H4 is shown to have a detrimental effect in cell proliferation and cause a global change of gene expression. These effects likely reflect CAF-1's functions in chromatin accessibility and heterochromatin integrity.

We demonstrate that the addition of short DNA oligomers promotes the dimerization of the CAF-1–H3-H4 complex. A cryo-EM structure of a 2:2 CAF-1–H3-H4 complex shows that the two H3-H4 heterodimers are placed nearby, with the H3 dimerization interface poised for interaction but not quite in the geometric configuration of an H3-H4 tetramer. Given that longer DNA fragments wrap H3-H4 as tetramers, the length of DNA may be a key factor in the CAF-1–mediated formation of H3-H4 tetramers. With a 147–base pair (bp) nucleosome-positioning Widom 601 DNA, we found that a right-handed CAF-1–bound ditetrasome was assembled through salt dialysis. This discovery was confirmed by single-molecule FOMT at a physiological salt concentration, indicating a possible unusual nucleosome precursor in chromatin replication.

CONCLUSION: Our study reveals the histone binding mode of CAF-1. It also elucidates the role of DNA in the dimerization of the CAF-1–H3-H4 complex and the assembly of H3-H4 tetramers and suggests the involvement of a right-handed nucleosome precursor in replication-coupled nucleosome assembly. ∎

Structures of CAF-1 with and without histones H3 and H4 bound. (Top middle) A 3.5-Å crystal structure of the core domain of CAF-1. Distinct subunits are labeled and color coded as indicated. The light pink segment with a dashed outline indicates disordered ED loop of p150. (Top left) A 3.5-Å cryo-EM structure of CAF-1 bound to a heterodimer of H3 (blue) and H4 (green). The light blue segment with a dashed outline indicates the disordered H3 loop that connects a short N-terminal segment and the body of H3. (Bottom left) A 4.6-Å cryo-EM map of a 2:2 CAF-1–H3-H4 complex in which CAF-1 subunits are colored gray. The graphic to the right of the arrow is a top view of the 2:2 dimer with CAF-1 omitted for viewing clarity. It shows the positioning of two H3-H4 heterodimers, shown in densities, in the 2:2 complex, compared with those in an H3-H4 tetramer, which is modeled by placing a fictitious H3-H4 dimer (ribbon representation) next to an observed one. (Top right) A 3.8-Å cryo-EM map of the CAF-1–bound right-handed ditetrasome compared with the left-handed DNA wrapping of a nucleosome core particle (NCP) schematically drawn at the bottom right corner.

READ THE FULL ARTICLE AT
https://doi.org/10.1126/science.add8673

STRUCTURAL BIOLOGY

Structural insights into histone binding and nucleosome assembly by chromatin assembly factor-1

Chao-Pei Liu[1]*†, Zhenyu Yu[1]†, Jun Xiong[1]†, Jie Hu[1]†, Aoqun Song[1]†, Dongbo Ding[1]†, Cong Yu[1,2], Na Yang[3], Mingzhu Wang[4], Juan Yu[1], Peini Hou[1], Kangning Zeng[1,5], Zhenyu Li[1], Zhuqiang Zhang[1], Xinzheng Zhang[1,5], Wei Li[1,5], Zhiguo Zhang[7], Bing Zhu[1,5,8]*, Guohong Li[1,5]*, Rui-Ming Xu[1,2,5]*

Chromatin inheritance entails de novo nucleosome assembly after DNA replication by chromatin assembly factor-1 (CAF-1). Yet direct knowledge about CAF-1's histone binding mode and nucleosome assembly process is lacking. In this work, we report the crystal structure of human CAF-1 in the absence of histones and the cryo–electron microscopy structure of CAF-1 in complex with histones H3 and H4. One histone H3-H4 heterodimer is bound by one CAF-1 complex mainly through the p60 subunit and the acidic domain of the p150 subunit. We also observed a dimeric CAF-1–H3-H4 supercomplex in which two H3-H4 heterodimers are poised for tetramer assembly and discovered that CAF-1 facilitates right-handed DNA wrapping of H3-H4 tetramers. These findings signify the involvement of DNA in H3-H4 tetramer formation and suggest a right-handed nucleosome precursor in chromatin replication.

The basic unit of chromatin is the nucleosome core particle (NCP), which consists of ~147 base pairs (bp) of DNA wrapped around an octamer of histones H3, H4, H2A, and H2B in a left-handed form (1). During DNA replication, nucleosomes are first disassembled to allow the progression of the replication fork and then reassembled to package newly synthesized DNA into chromatin (2, 3). Half of the histones for nucleosome assembly are of parental origin, and they are segregated onto two nascent DNA duplexes, mostly in the form of H3-H4 tetramers (4–6). The other half of the histones are newly synthesized in S phase of the cell cycle and are deposited onto DNA in a stepwise process known as de novo assembly, in which newly synthesized histones H3 and H4 are first deposited onto DNA to form tetrasomes, followed by the addition of two histone H2A-H2B dimers to form the NCP. The evolutionarily conserved chromatin assembly factor-1 (CAF-1) complex is responsible for DNA replication–coupled nucleosome assembly, which is essential for genome integrity and epigenetic inheritance (7–9). Despite much progress, further breakthroughs in structure and function studies of CAF-1, including its histone binding mode, are needed to fully comprehend the mechanism by which chromatin is faithfully inherited.

CAF-1 was discovered based on its ability to promote de novo nucleosome assembly during in vitro replication of SV40 DNA templates (7). It binds newly synthesized H3.1-H4 histones and facilitates their deposition at the replication fork during S phase in cooperation with histone H3-H4 chaperone ASF1 and the replication processivity factor proliferating cell nuclear antigen (PCNA) (10–13). Human CAF-1 is essential for replication-coupled chromatin assembly in vivo (14), but disruption of the corresponding yeast complex does not obviously affect cell growth (15, 16). This is likely due to the presence of alternative chromatin assembly pathways in yeast (12, 13, 17–19). Additionally, CAF-1 plays important roles in chromatin repair after ultraviolet light–induced DNA damage (20, 21) and in cell fate determination and maintenance (2, 22).

Human CAF-1 is composed of p150 (CHAF1A), p60 (CHAF1B), and p48 (RBBP4/RbAp48) subunits (9, 23). p150 contains various motifs for interacting with the replication machinery and chromatin factors, including the DNA-binding KER and WHD domains and the highly acidic ED region that is implicated in histone binding (21, 24, 25) (Fig. 1A). The N-terminal region of p150 was shown to be dispensable, whereas the middle and the C-terminal regions are important for binding histones and p60, respec-

tively (9). Both the p60 and p48 subunits are WD40-repeat proteins that are known to form a β-propeller scaffold (Fig. 1A). p60 plays important roles in DNA synthesis and repair and participates in the progression of various malignancies (26–28). It contains a C-terminal ASF1-interacting motif (B domain) that may facilitate the transfer of H3-H4 to CAF-1 (29). Importantly, p60 directly binds H3-H4 and is required for CAF-1's nucleosome assembly activity (9, 30). p48 is a versatile histone H3-H4 chaperone found in numerous histone-modifying enzymes and nucleosome-remodeling complexes (23, 31). It is conceivable that it may couple CAF-1's function in nucleosome assembly with the installation of histone modifications (32, 33).

Until now, inadequate knowledge about the structure of CAF-1 severely limited mechanistic understandings of de novo nucleosome assembly (30, 34–36). In this work, we have determined the crystal structure of the human CAF-1 core complex and cryo–electron microscopy (cryo-EM) structures of CAF-1 bound to H3-H4. Interestingly, we also observed a complex of CAF-1 bound to a right-handed H3-H4 ditetrasome, implicating an unexpected step in nucleosome assembly.

Results

Overall structure of the CAF-1 complex

We first tried to crystallize the CAF-1 complex with full-length p150 or its truncation variants p150M, which contains the middle domain encompassing the ED region and its N- and C-terminal flanking regions (NTR and CTR, respectively), and p150L, which has a longer C-terminal extension (Fig. 1A). These complexes were coexpressed in insect cells and purified to apparent homogeneity (Fig. 1B), but only the complex with p150M, p60 with a C-terminal 140-residue deletion (p60ΔC), and full-length p48, termed CAF1-MC was crystallized. Three structures from distinct crystal forms (C222₁, C2, and P2₁) at 3.4- to 3.6-Å resolutions were solved (fig. S1A and table S1), and they all have a 1:1:1 subunit stoichiometry. p150M exhibits an extended conformation, with its ordered portions of NTR (residues 463 to 606) and CTR (residues 658 to 713) binding p48 and p60, respectively (Fig. 1C). An ~50-residue region connecting the NTR and CTR is disordered, and this results in an ambiguity in distinguishing two crystallographically equivalent models (Fig. 1C and fig. S1B). In model 1, the p48 and p150 NTR globular module makes little contact with the p60-p150 CTR module (Fig. 1C); in model 2, the two modules are close together, and an NTR segment (residues 524 to 542) interacts with p60 (fig. S1, B and C). Glutathione S-transferase (GST)–pulldown results show that the p150 NTR and CTR fragments only pulled down p48 and p60 separately (fig. S1D), thus disfavoring the model 2 packing. Thus, we used model 1 for further analysis.

[1]National Laboratory of Biomacromolecules and Key Laboratory of Epigenetic Regulation and Intervention, Institute of Biophysics, Chinese Academy of Sciences, Beijing 100101, China. [2]Key Laboratory of Systems Health Science of Zhejiang Province, School of Life Science, Hangzhou Institute for Advanced Study, University of Chinese Academy of Sciences, Hangzhou, Zhejiang 310024, China. [3]State Key Laboratory of Medicinal Chemical Biology, College of Pharmacy and Key Laboratory of Medical Data Analysis and Statistical Research of Tianjin, Nankai University, Tianjin 300353, China. [4]Institutes of Physical Science and Information Technology, Anhui University, Hefei, Anhui 230601, China. [5]School of Life Sciences, University of Chinese Academy of Sciences, Beijing 100049, China. [6]School of Physical Sciences, University of Chinese Academy of Sciences, Beijing 100049, China. [7]Institute for Cancer Genetics, Department of Pediatrics and Department of Genetics and Development, Columbia University Irving Medical Center, New York, NY 10032, USA. [8]New Cornerstone Science Laboratory, Institute of Biophysics, Chinese Academy of Sciences, Beijing 100101, China.
*Corresponding author. Email: liuchaopei@ibp.ac.cn (C.-P.L.); zhubing@ibp.ac.cn (B.Z.); liguohong@ibp.ac.cn (G.L.); rmxu@ibp.ac.cn (R.-M.X.)
†These authors contributed equally to this work.
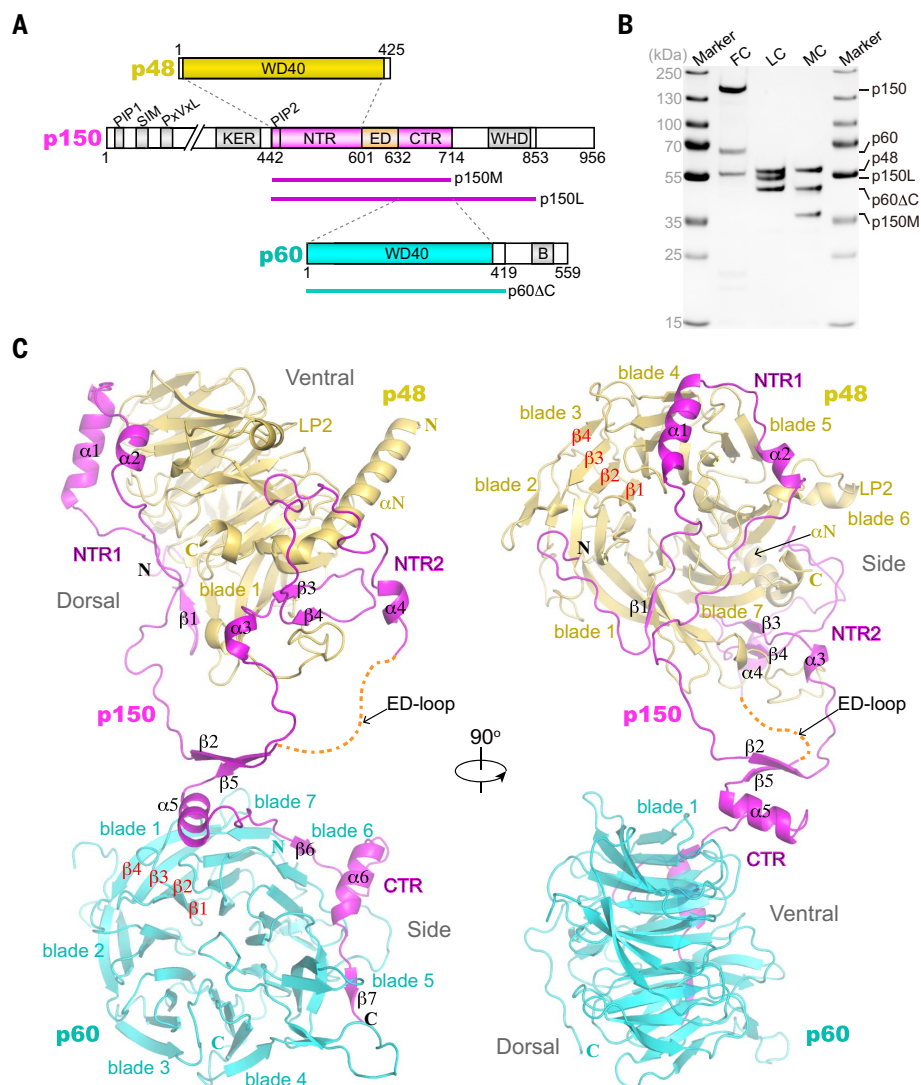
Fig. 1. Crystal structure of CAF-1. (**A**) Domain structures of CAF-1 subunits. The core domains of p48, p150, and p60 are colored amber, magenta, and cyan, respectively. Line segments that are colored the same as the protein domains indicate protein fragments used in this study. Dashed lines indicate protein regions involved in pairwise interactions. (**B**) Coomassie blue–stained SDS–polyacrylamide gel electrophoresis (SDS-PAGE) analysis of purified recombinant CAF-1 complexes. Displayed are CAF1-FC; CAF1-LC, containing p150L, p60ΔC, and p48; and CAF1-MC, containing p150M, p60ΔC, and p48. (**C**) Crystal structure of CAF-1. Different subunits are colored according to the scheme in (A), and the orange dashed line denotes the disordered ED domain of p150. The seven blades of the p48 and p60 β propellers, from the N- to C-terminal direction, are numbered from 1 to 7. Four strands in each blade are numbered from β1 to β4, as illustrated in blade 1 of p60 and blade 3 of p48.

The p150 NTR is anchored to two disjoint surface patches on p48. One p150 binding region occupies a large surface area on the wider base of the p48 β propeller, termed the dorsal face (Fig. 1C). The N-terminal portion of p150 NTR, which encompasses residues ~463 to 533 and is designated NTR1, is composed of a short β strand (β1), two α helices (α1 and α2), and irregular loop segments. NTR1 does not have a compact core, and it snakes across the dorsal surface of p48 mainly through hydrophobic interactions. The second p48-interacting region of p150 NTR, called NTR2, approximately spans residues 548 to 606 and is connected to NTR1 by an ~15-residue linker that is not interacting with either p48 or p60. NTR2 contains two short α helices (α3 and α4) and a pair of short β strands (β3 and β4). NTR2 interacts with p48 through parallel β pairing between its β3 and the outmost strand of p48's blade 7, as well as through its β3-β4 and β4-α4 loops, which are arranged like a pair of claws, gripping on the C-terminal portion of the αN helix of p48 (Fig. 1C). The combined interactions

through NTR1 and NTR2 stably anchor the NTR of p150 onto p48.

p60 is a seven-bladed β propeller characterized by a long β-hairpin insertion between β4 of blade 4 and β1 of blade 5 on the ventral surface, a long β-loop insertion between β1 and β2 of blade 6, and a long C-terminal tail that traverses the dorsal surface of the β propeller (Fig. 1C). The CTR of p150 interacts with p60 through two α helices (α5 and α6) and two β strands (β6 and β7), whereas its β5 makes an intramolecular β pairing with β2 of NTR. α5 of p150 CTR interacts with p60 mainly through polar interactions with three loop segments of p60 that line the ventral edge of the β propeller. The β6-α6-β7 cassette of p150 CTR makes extensive interactions with blades 5 and 6 of the p60 β propeller, with β6 and β7 making antiparallel β pairings with β4 strands of blade 6 and blade 5 of p60, respectively, whereas α6 and its flanking loop segments primarily interact with blade 6 (Fig. 1C).

The bilobal organization of the CAF-1 core complex indicates considerable conformational plasticity between the two globular modules, suggesting that dynamic relative positioning of p48 and p60 may be intrinsic to CAF-1's histone binding and nucleosome assembly activities.

Structure of CAF-1 bound to histone H3-H4

Extensive cocrystallization trials of H3-H4 with full-length and truncation mutants of CAF-1, which were tested by GST-pulldown and DNA supercoiling assays (fig. S2), were unfruitful. We then resorted to single-particle cryo-EM for structure determination and succeeded in determining the structures of the full-length CAF-1 complex (CAF1-FC) and CAF1-LC, a CAF-1 complex consisting of p150L that includes the WHD domain, full-length p48, and p60ΔC (Fig. 1B and fig. S2B), bound to a heterodimer of histones H3-H4 at 3.6- and 3.8-Å resolutions, respectively (figs. S3 and S4 and tables S2 and S3). Representative EM map sections of various parts of the 3.8-Å structure are shown in fig. S5. The two structures are highly similar in ordered regions and their spatial arrangements; their EM maps can be superimposed with a correlation coefficient of 0.976, and the datasets can be combined to yield a map of 3.5 Å (fig. S4 and table S3). Henceforth, instead of specifying the structures determined using the full-length CAF-1 complex (CAF1-FC) or the longer fragment CAF-1 complex (CAF1-LC), we will collectively refer to the two structures as CAF-1 for clarity of description, unless explicitly noted. In the structure, only the core region of p150, approximately spanning residues 491 to 713, and the WD40 domains of p60 (residues 1 to 392) and p48 (residues 11 to 411) are ordered (Fig. 2, A and B), generally corresponding to the CAF-1 core in the crystal structures. No densities for other parts of CAF-1 can be located, indicating

Fig. 2. Cryo-EM structure of CAF-1 bound to H3-H4. (**A**) Front (top) and back (bottom) views of the density map, which is sharpened with a B-factor of −144 Å² and contoured at 4.0σ. CAF-1 subunits are colored the same as in Fig. 1C, and H3 and H4 are shown in dark blue and green, respectively. (**B**) A cartoon model of the CAF-1–H3-H4 complex structure in the front view. p150 is highlighted with the superposition of a semitransparent surface representation of the density. Disordered internal loops are represented with dashed lines. (**C**) A back view of the superimposed apo crystal structure and the H3-H4–bound cryo-EM structure of CAF-1 through alignment of p60. The crystal structure is colored with p150 in periwinkle and p60 and p48 in gray; the cryo-EM structure is colored the same as in (B). Histones H3-H4 are represented by a pale bicolor ellipse for viewing clarity. Paired arrow lines indicate the relocation of the same structural elements of p150 and p48 in the two structures. Transformation of the β5-α5 unit of p150 in the crystal structure into part of α5B in the cryo-EM struc-

ture is indicated by a dashed arrow arc. See also movie S1. (**D**) An overview of the interaction between CAF-1 and histones H3-H4. The exposed histone H3-H4 tetramerization interface is indicated by the black triangle. (**E**) A schematic drawing depicting the overall features of H3-H4 binding by CAF-1.
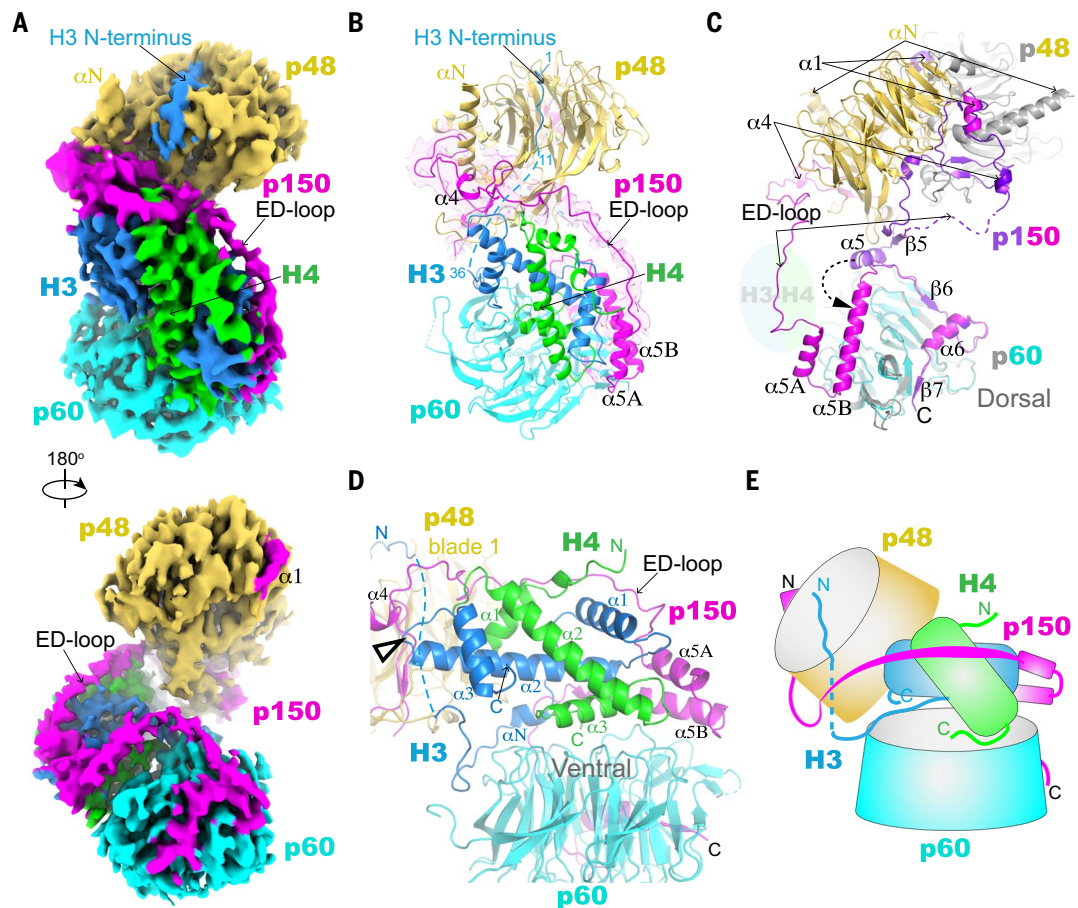
that they are flexibly positioned relative to the CAF-1 core and that their interactions with H3-H4, if any, are dynamic and/or heterogeneous. There is also no density for a 30-bp DNA oligomer (DNA_{30}), which was added as a buffering reagent to alleviate histone precipitation at low-salt concentrations during cryo-EM sample preparation.

All three subunits of CAF-1 are involved in direct interaction with the H3-H4 heterodimer (Fig. 2, A and B). Compared with the crystal structure, the p48 and p60 modules showed little changes, but a large rearrangement of their relative positioning occurred (Fig. 2C and movie S1). Superimposing p60 from the two structures as a reference, p48 is rotated and located further away from p60 in the apo crystal structure than in the complex with H3-H4. For example, two p150 α4s from the two structures are located ~70 Å apart (Fig. 2C and movie S1). Through this substantial conformational change upon H3-H4 binding, the NTR1 region of p150 that interacted with p48 becomes largely disordered, with only a portion of α1 remaining visible. The linker between NTR1 and NTR2 is also disordered, but NTR2 binds p48 in the same manner as in the apo

structure (Fig. 2B). The ~50-residue loop connecting NTR and CTR of p150, including the highly negatively charged ED loop, becomes ordered upon H3-H4 binding (Fig. 2A and fig. S5B). Within the CTR region of p150, the β6-α6-β7 cassette bound p60 essentially the same in the two structures (Fig. 2C). However, β5 is dissolved and joins α5 to form a longer α5B helix that orients in a direction opposite to the original α5 and rests on top of the ventral surface of p60, together with a newly ordered α5A that lies antiparallel to α5B (Fig. 2C and fig. S5B).

The ordered H3 regions include residues 1 to 11 and 36 to 134, whereas those of H4 include residues 21 to 101 (Fig. 2B and fig. S5B). With the exception of the first 11 residues of H3, which bind p48 in the same manner as they bind to other RbAp46/48 homologs (33), H3-H4 binds CAF-1 in a new fashion. H3-H4 is stably positioned above the ventral surface of the p60 propeller by means of extensive interactions involving H4's C-terminal part, from the penultimate turn of α2 (Tyr^{72}) onward (Fig. 2D). Furthermore, an H3 region encompassing residues 40 to 55, which includes a partially unfolded αN, wraps around a contig-

uous perimeter margin of the p60 β propeller spanning blades 6, 7, and 1. With p150's NTR and CTR firmly anchored on p48 and p60, respectively, the ED domain of p150 adopts an extended conformation and binds H3-H4 by traversing the positively charged convex surface of H3-H4 that is formed by the α1 helices of H3 and H4 (Fig. 2D). The newly formed α5A and α5B of p150 are positioned above the ventral surface of p60 and contact the α2-α3 loop of H4, the α1-α2 loop, and the partially unfolded αN region of H3. Intuitively, one may imagine that CAF-1 subunits house the binding of H3-H4 like a car seat (Fig. 2E), with the ventral surface of p60 as the seat, the long positively charged ED loop of p150 as the seatbelt, α5A and α5B of p150 as the guardrail, and the side of p48 as the headrest, against which the C-terminal end of H3's α2 and the α1-α2 loop of histone H4 rest.

Interaction between p150 and histones H3-H4

The ED loop of p150 (residues 601 to 632) interacts extensively with both histones H3 and H4 (Fig. 2D). The rest of the interaction mainly involves α5A and α5B, which are located immediately C-terminal to the ED loop. Two-thirds

of the ED-loop residues are negatively charged, and they interact with H3-H4 following a trail of positively charged residues located on the curved back of the H3-H4 heterodimer, which is mainly formed by the α1 helices of H3 and H4 that are normally involved in binding DNA in the nucleosome (Fig. 3A). The charge interaction between the ED loop of p150 and H3-H4 is somewhat reminiscent of that between the histone chaperone domain of MCM2 and H3-H4 (fig. S6A) (37–39), indicating a common strategy for safeguarding H3-H4 from promiscuous interaction with DNA during DNA replication. The vast overlapping binding area of CAF-1 and MCM2 on H3-H4 may protect their binding fidelity toward nascent and parental histone H3-H4s, respectively (40).

The main-chain model of the 32-residue, surface-exposed ED loop fits the continuous cryo-EM map well, but weaker side-chain densities limited precise identification of specific interactions between the ED loop and histones H3-H4 (fig. S5B). To circumvent this problem, we carried out bloc mutations on both the ED loop and histones to test their interactions. The N- and C-terminal halves of the ED loop, ED-N1 (residues 601 to 617) and ED-C1 (residues 618 to 632), and a longer C-terminal fragment, ED-C2 (residues 617 to 646) that includes α5A, were replaced with equal-length GS linkers, which are tandem penta-peptide repeats consisting of four contiguous glycine residues and a serine (Fig. 3A). Helix α5A interacts with the α1-α2 loop of H3 and the α2-α3 loop of H4 (Fig. 2D). GST-pulldown (Fig. 3B) and in vitro supercoiling (Fig. 3C and fig. S6B) assays showed that the ED-C1GS and ED-C2GS substitutions weakened the histone binding and nucleosome assembly abilities of CAF-1, to degrees comparable to that when the entire ED-loop was substituted (EDGS), whereas the ED-N1GS substitution displayed less appreciable effects. Amino acid substitution of four negatively charged residues in ED-C1 [denoted 4mut, with substitutions E628K (Glu^{628}→Lys), D629N, E630K, and D632G] displayed even weaker effects in the GST-pulldown and supercoiling analyses (Fig. 3, B and C). Furthermore, because ED-N1 mainly interacts with histone H4 and ED-C1 and ED-C2 with H3 (Fig. 3A), we probed reciprocal interactions using H3 and H4 mutants. Alanine substitutions of the ED loop–interacting residues Arg^{63}, Arg^{69}, and Arg^{83} of histone H3 (H3-3A) and Arg^{35}, Arg^{39}, and Lys^{44} of histone H4 (H4-3A) were generated, and the H3-3A and the combined H3-3A H4-3A (6A) mutant complexes exhibited weakened binding to CAF-1 compared with the wild-type (WT) H3-H4 complex, whereas the H4-3A complex only displayed subtle effects (fig. S6C). These results support the structural model of p150-histone interaction and highlight the importance of the interaction between the C-terminal portion of the ED loop and histone H3.

CAF-1's replication-coupled (RC) nucleosome assembly activity directly affects nucleosome occupancy behind the replication fork and is also required for optimal gene silencing and S phase progression (14–16, 41). Therefore, we used two methods to analyze the cellular effects of relevant CAF-1 mutants: (i) a modified ReIN-Map (replication-intermediate nucleosome mapping) method combined with MINCE-seq [mapping in vivo nascent chromatin with 5-ethynyl-2′-deoxyuridine (EdU) sequencing] (42, 43) and (ii) transcriptome analysis together with a cell proliferation assay. We first established p150 and p60 auxin-inducible degron (AID) HAP1 cell lines by CRISPR-Cas9–mediated knock-in, with which the AID-tagged p150 or p60 proteins could be degraded within hours after 5-phenyl-indole-3-acetic acid (5-Ph-IAA) treatment (44) (fig. S6D). We then introduced doxycycline-inducible exogenous p150 constructs into the p150-AID cell line by lentiviral transduction (fig. S6E). The cells cannot survive prolonged p150 depletion by treating with the auxin analog 5-Ph-IAA (6 days), and we found that the p150 ED-loop replacement mutants affect cell proliferation to degrees analogous to the levels to which they influence histone binding, with the 4mut substitution mutant showing the least growth defect (Fig. 3D). Analysis of RC nucleosome assembly was performed following a procedure schematically outlined in Fig. 3E. Analyses of EdU-labeled nucleosome occupancies surrounding transcription start sites (TSSs) and CTCF-binding sites showed again that the p150 ED-loop mutants differentially affect RC nucleosome assembly in a manner dependent on their histone binding abilities (Fig. 3F). By comparison, steady-state nucleosome occupancy is little affected (fig. S6F). Depletion of the CAF-1 subunits has been well documented to induce derepression of silenced genes, likely because of impairment of heterochromatin formation (16, 45). Therefore, gene derepression analysis is a good surrogate for CAF-1 function in chromatin assembly. RNA sequencing (RNA-seq) analyses revealed that induced degradation of p150 leads to elevated expression of ~2500 genes, in contrast to the ~250 down-regulated genes, which is consistent with the functional role of CAF-1 in heterochromatin formation and silencing. Rescue with exogenous WT p150 restored ~80% of expression patterns of WT AID cells (fig. S6G). The C1GS, C2GS, and EDGS mutants showed obvious defects (~30 to 40%), whereas the 4mut substitution mutant functioned nearly as well as the WT p150 (fig. S6G).

p60-histone interaction and implication for oligomeric states of H3-H4

p60 interacts with H3 and H4 primarily through its ventral surface area. The central area of the ventral surface is enriched with negatively charged residues, together with several tyrosines

and a phenylalanine. It hosts extensive interactions with H4 residues located at the C-terminal end of α2, the entire α3, and the following C-terminal tail (Figs. 2D and 4A). In particular, Tyr^{88} and Lys^{91}, which are located on α3 of H4, insert into the central basin of the ventral surface of p60 (Fig. 4A). Tyr^{88} is surrounded by hydrophobic residues Tyr^{133}, Tyr^{173}, and Phe^{236} of p60, whereas Lys^{91} is positioned within bonding distances from Asp^{86} and Asp^{131} of p60. Recurrent missense mutations of H4 residues Lys^{91}, Tyr^{98}, and His^{75}, which are all located on the interface with p60, are found in a neurodevelopmental syndrome (46), whereas an Asp-to-Asn substitution of Asp^{86} (D86N) of p60 is found in somatic cancer mutations tabulated in the Catalogue of Somatic Mutations in Cancer (COSMIC) database. GST-pulldown and supercoiling assays of the p60 D86N mutant complex of CAF-1 showed no obvious defects (fig. S7, A and B), likely because, owing to the extensive p60-H4 interaction, a single D86N change is not sufficient to yield detectable effects in vitro. Nevertheless, we examined the cellular effect of this mutation using the p60 AID cell line (figs. S6D and S7C). The p60 D86N mutant caused a severe growth defect (Fig. 4B), suggesting its functional importance. Induced degradation of p60 increased the expression of 681 genes (Fig. 4C). The differential effects in cell growth and gene expression between the WT and D86N p60 may be largely attributed to the amino acid difference, because WT and D86N p60, and also p150, were expressed at comparable levels (fig. S7C), notwithstanding the reduction of p150 upon p60 degradation in the absence of exogenous p60 (fig. S6D), as also previously reported (47, 48). Of the up-regulated genes from p60 degradation, 87% coincide with those from p150 degradation, consistent with their shared function in the same protein complex. Even those genes not belonging to the common set changed in the same direction (fig. S7D). Finally, ReIN-Map analysis revealed no obvious change by the p60 D86N mutation (fig. S7E), suggesting possible involvement in chromatin accessibility and heterochromatin integrity (16, 45, 47, 49, 50).

Besides H4, a partially unwound αN of H3 lies in a negatively charged channel on the p60 surface, with H3 Tyr^{54} interacting with Tyr^{346}, Asp^{367}, and Tyr^{369} and H3 Arg^{49} contacting Glu^{7} and Tyr^{369} of p60 (Fig. 4D). The H3 loop segment spanning residues 40 to 48 binds a positively charged surface patch located at the edge of the ventral surface of p60. In this binding manner, the dimerization interface of histone H3 is fully exposed (Fig. 2D). However, binding to an H3-H4 tetramer is prohibited, owing to steric clashes between p60 and histone H4 from a modeled second heterodimer (Fig. 4E). These observations reveal a mechanism of safeguarding premature H3-H4 tetramer
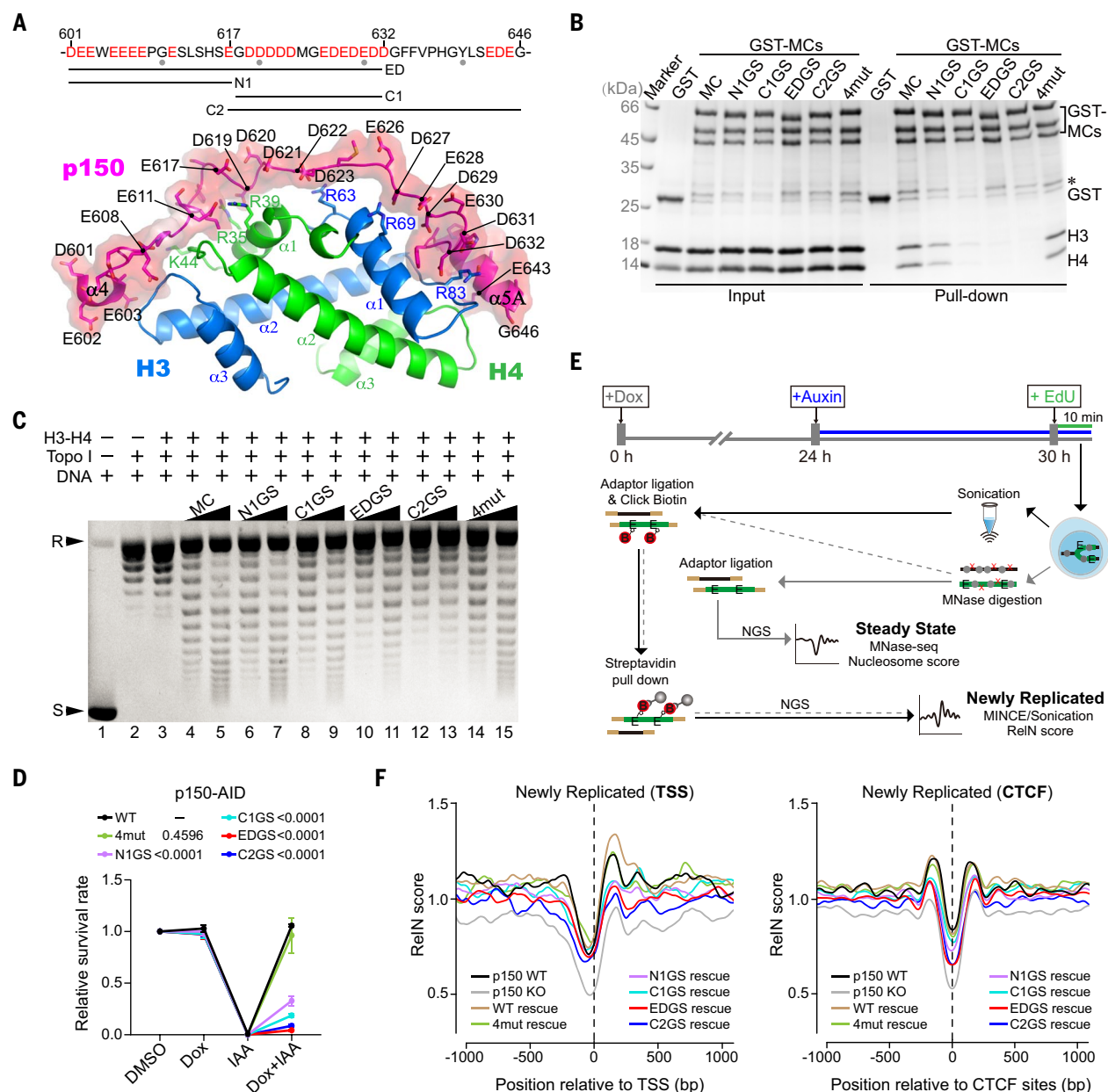
Fig. 3. Interaction between p150 and histones H3-H4. (**A**) Detailed view of the interaction between the ED domain of p150 and histones H3-H4. Shown at the top is the amino acid sequence of the ED domain, with acidic residues colored in red, and the designation of different fragments for functional analyses. Shown at the bottom is the interaction between key acidic residues in the ED domain of p150 and H3-H4. D, Asp; E, Glu; G, Gly; K, Lys; R, Arg. (**B**) Pulldown of H3-H4 with GST-tagged CAF1-MC complexes with an intact p150M or mutants substituting the ED-domain fragments in (A) with equal-length GS linkers; for example, N1GS and EDGS mutants substitute the N1 fragment and the entire ED domain with GS linkers, respectively. 4mut represents the E628K/D629N/E630K/D632G quadruple mutation in p150M. Pulldowns were performed at 1 M NaCl and analyzed by Coomassie blue–stained SDS-PAGE. The asterisk indicates an unidentified contaminant band. (**C**) Supercoiling assay of in vitro nucleosome assembly by CAF-1. ϕX174 DNA (lane 1) was treated with DNA topoisomerase I (Topo I, lane 2) and incubated with H3-H4 only (lane 3) or increasing amounts (0.1 and 0.2 μg) of WT or indicated mutants of CAF1-MC (lanes 4 to 15), together with 0.1 μg of H3-H4 and 0.1 μg of relaxed ϕX174 DNA. R and S at the left indicate the position of relaxed and supercoiled DNA, respectively. Input protein samples are shown in fig. S6B. (**D**) Cell

proliferation activities of WT p150 or its mutants in p150-AID cells, which were first treated with doxycycline (Dox) to induce the expression of exogenous p150 constructs. 5-Ph-IAA was added 24 hours after Dox treatment. Cell viability was measured by CellTiter-Glo after 7 days of Dox treatment. Error bars represent SEM calculated from three biological replicates. Two-way analysis of variance (ANOVA) with Sídák test was used to calculate the *p* values shown at the top of the figure. (**E**) Schematic of the ReIN-map and MNase-seq protocol. Cells were treated with Dox, Auxin, and EdU at the indicated time points, and chromatin was cross-linked and sheared either by MNase digestion or sonication. DNA of MNase-treated samples was extracted and ligated with next-generation sequencing (NGS) adaptors, and the MNase-seq signals reflect the steady-state nucleosome occupancy. For ReIN-map, DNA of MNase-treated and corresponding sonication-sheared samples were extracted and ligated with NGS adaptors. EdU-labeled newly replicated regions were biotinylated and separated with streptavidin beads. The ReIN score was derived by dividing the MINCE-seq signals by the Sonication-seq signals. (**F**) The ReIN scores for regions around the TSSs (left) and the CTCF-binding sites (right) are shown. The CTCF chromatin immunoprecipitation sequencing (ChIP-seq) data are from the Gene Expression Omnibus (GEO; GSM4640493) (*81*).
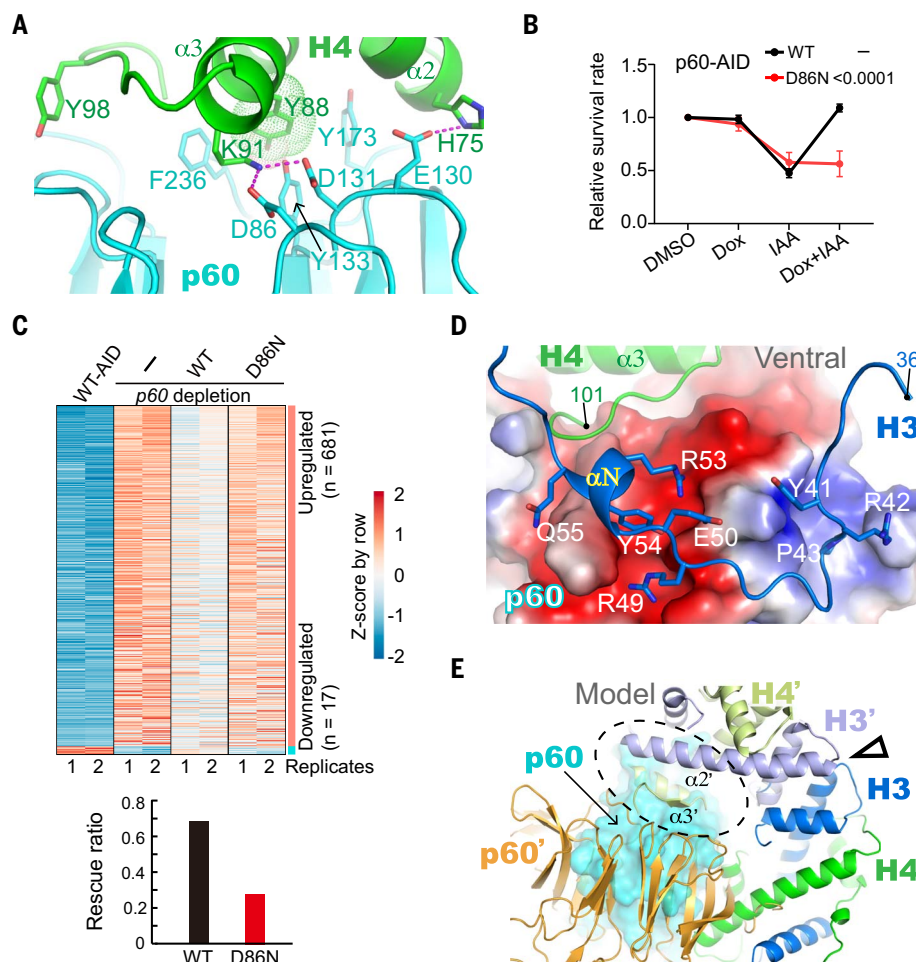
Fig. 4. Interactions between p60 and histone H3-H4. (**A**) Histone H4–p60 interaction at the center of the ventral surface of p60. Involved residues are shown in a stick model. Magenta dashed lines indicate potential hydrogen bonds. Tyr[88] of H4, which is situated in the central basin of the ventral face of p60, is superimposed with a dots model. F, Phe; P, Pro; Q, Gln; Y, Tyr. (**B**) Cell proliferation activity of WT p60 and the D86N mutation assayed in the same was as in Fig. 3D. Error bars represent SEM from three biological replicates. (**C**) Heatmaps showing differentially expressed genes (DEGs) in p60-depleted and rescued cells versus WT-AID HAP1 cells. Two biological replicates were performed for each experiment. The bottom panel shows the rescue ratios of transcriptional changes, which is defined as $1 - [\#(A \cap B)]/[\#(A)]$, where A is the set of DEGs from p60 depletion and B is the set of DEGs from rescue expression of WT or D86N p60 constructs. The # function gives the number of genes in the set. (**D**) Interaction between histone H3 (dark blue) and p60. Histones H3-H4 are drawn in a cartoon model, with involved H3 residues depicted in a stick model. p60 is shown in a surface model colored according to electrostatic potential (negative, red; neutral, white; positive, blue) with the display range of −3 to +3 k_BT/e, where k_B is the Boltzmann constant and T and e are the temperature and electron charge in SI units, respectively. (**E**) Docking of a second CAF-1–H3-H4 complex (p60′, orange; H3′, light blue; H4′, light green) to model the formation of a H3-H4 tetramer between the H3′-H4′ heterodimer and the H3-H4 heterodimer from the first CAF-1–H3-H4 complex, which is colored as in Fig. 2B, results in steric clashes between H4′ and p60 (indicated with a dashed oval), and p60′ with p60 and H4. The black triangle indicates the H3-H3′ dimerization interface. p150 and p48 have been removed for viewing clarity.

formation by a histone H3-H4 chaperone, which differs from the mechanisms of maintaining H3-H4 in a dimeric form through the blocking of the dimerization interface by other H3-H4 chaperones (*51*).

Assembly of two nascent H3-H4 dimers into a tetramer has important implications for epigenetic inheritance, and the prevailing assumption is that H3-H4 heterodimers bound by two CAF-1 complexes will be spontaneously assembled into a tetramer (*24*). We observed a small percentage of particles with two CAF-1s bound to two H3-H4 heterodimers in the cryo-EM samples of both the LC and full-length complexes of CAF-1 bound to H3-H4 (figs. S3 and S4). The cryo-EM map calculated from combining the CAF-1 LC and FC datasets has an overall resolution of 4.6 Å, allowing reliable

placement of two CAF-1–H3-H4 complexes (Fig. 5A and figs. S3 and S4). A SEC-MALS (size exclusion chromatography coupled to multiangle light scattering) analysis shows that the addition of 30-bp DNA, which was used in our cryo-EM sample preparation, promoted the dimerization of CAF-1–H3-H4 complexes, regardless of whether the MC, LC, or FC complex of CAF-1 was used (Fig. 5B and fig. S8). As in the cryo-EM reconstruction of the monomeric CAF-1–H3-H4 complex, we do not see the density of DNA here either. The structure shows that a pseudo twofold symmetry relates the two CAF-1–H3-H4 complexes. In this arrangement, the two p60s are juxtaposed, and a positively charged surface patch located on the side of the p60 propeller, which is formed by residues from the loop segments C-terminal to the β4 strands of blades 1 and 2 and the β3-β4 loop of blade 3, contacts the C-terminal portion of α2 of H4 from the other complex (Fig. 5C). The homodimerization interface on two H3s are facing each other but not oriented in the same way as in an H3-H4 tetramer (Fig. 5D). The two H3-H4 heterodimers in the structure appear to be "nearly" able to form a tetramer, but it is obstructed by the presence of p60. A remodeling of the observed p60-histone interaction, perhaps with the help of a longer DNA, would fulfill the assembly of an H3-H4 tetramer, which is believed to be the unit for CAF-1 deposition (*8*, *35*, *52*).

CAF-1 facilitates the assembly of a right-handed ditetrasome

Deposition of H3-H4 onto DNA by CAF-1 is believed to lead the formation of a tetrasome containing DNA and an H3-H4 tetramer. To gain further insights, we tried tetrasome assembly for structural characterization by salt dialysis in vitro. We initially dialyzed CAF1-LC, histone H3-H4, and a 147-bp Widom 601 DNA together from 2 M to 50 mM NaCl, and two major peaks, peak 1 and peak 2, appeared in cryo-EM sample preparation by GraFix (fig. S9A). From the peak 1 sample, the structures of a left-handed ditetrasome and a CAF-1–bound right-handed ditetrasome were determined at 3.5- and 3.8-Å resolutions, respectively (fig. S9, B to F; and table S2). The peak 2 sample predominantly shows a right-handed ditetrasome bound by two CAF-1 complexes, and the structure was determined at 5.6 Å (fig. S10 and table S2). The left-handed ditetrasome structure is nearly identical to the recently reported H3-H4 octasome structure (*53*); hence, we will not discuss it further here. We then repeated the cryo-EM procedures using the full-length CAF-1 complex and obtained similar results (fig. S11 and table S3). Cryo-EM reconstructions of a right-handed ditetrasome with one and two CAF-1 bound were obtained at 3.8- and 6.6-Å resolutions, respectively. Both
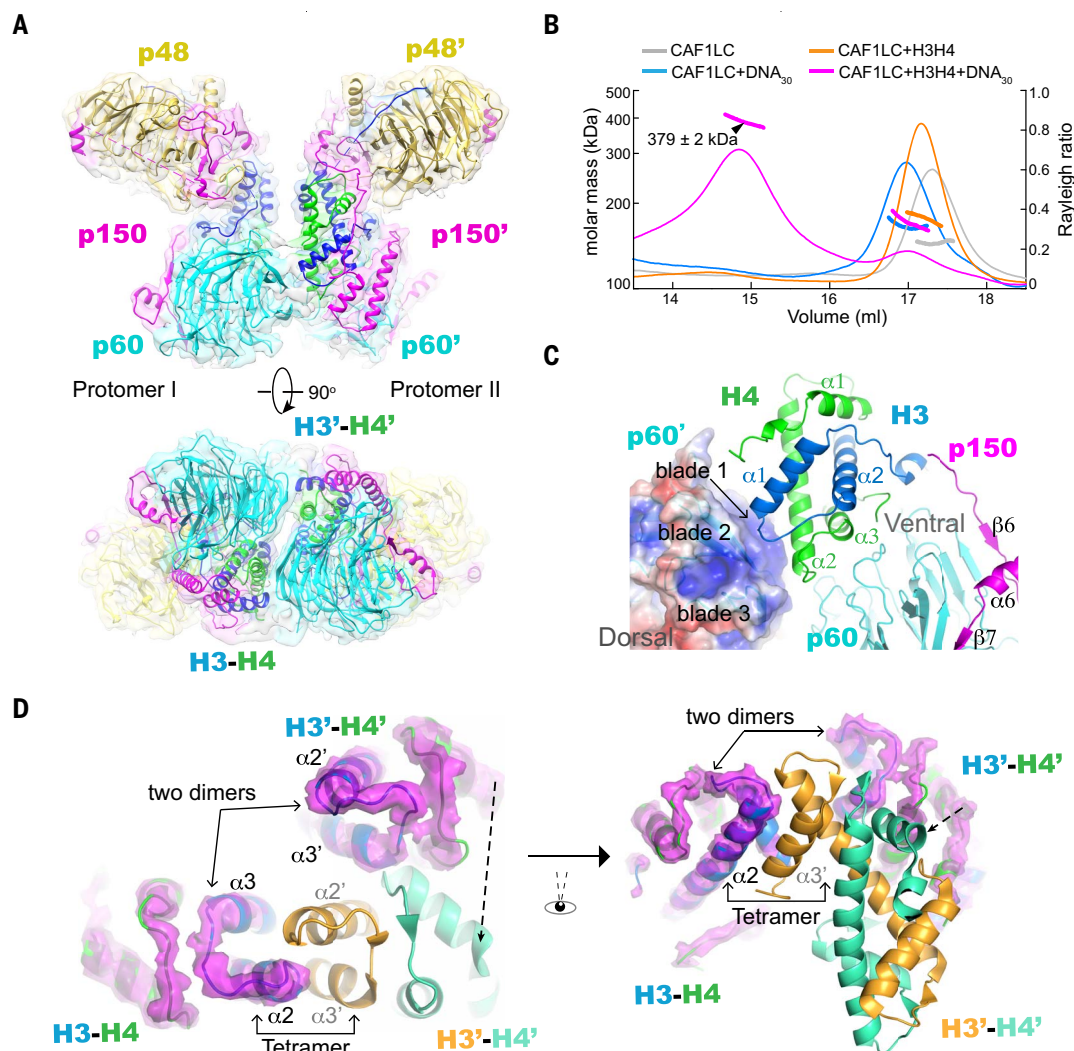
Fig. 5. A 2:2 complex of CAF-1 and H3-H4. (**A**) Two views of the 4.6-Å composite cryo-EM density map of the 2:2 complex contoured at 3.4σ superimposed with the structure model. The coloring scheme is the same as in Fig. 2A. (**B**) SEC-MALS analysis of CAF1-LC and its complex with H3-H4, in the presence and absence of 30-bp DNA. The SEC profile (thin lines) is superimposed with the fitted MALS results (short thick lines) according to the colors specified at the top of the figure. The 379 ± 2–kDa peak from the CAF1-LC–H3-H4–DNA_{30} sample indicates the formation of a 2:2 complex (calculated mass ~377 kDa). (**C**) Interactions between histone H3-H4 of one CAF-1–H3-H4 complex and p60' of another complex, which is shown as the electrostatic potential surface (color range, −3 to +3 k_BT/e). H3-H4 binds a positively charged region spanning blades 1 to 3 of p60'. (**D**) Two views of the mismatched H3 dimerization areas, which are indicated by a pair of arrows labeled "two dimers," in the 2:2 complex. The two H3-H4 heterodimers from the cryo-EM structure are shown in a cartoon model superposed with a magenta semitransparent density map. For comparison with the face-to-face placement of two H3 dimerization surfaces in a tetramer, an additional H3-H4 heterodimer (cartoon model with H3' in bright orange and H4' in green cyan) is modeled onto one of the H3-H4 heterodimers in the 2:2 complex. The tetramer interface is indicated by a bidirectional arrow line labeled "tetramer."

the one–CAF-1–bound and the two–CAF-1–bound ditetrasome structures from the LC and FC complexes of CAF-1 are highly similar (fig. S11, E and F). Therefore, we will use the structures obtained from the CAF1-LC for the discussion that follows.

In the CAF-1–bound right-handed ditetrasome, a 108-bp DNA segment wraps around two overlapping H3-H4 tetramers ~1.5 times in a right-handed manner (Fig. 6A and fig. S12). Each H3-H4 tetramer binds DNA similarly to that in the nucleosome, except at the border of two tetramers, where the α2-α3 ends of H4s from two tetramers move in opposite

directions laterally and closer longitudinally (Fig. 6B). As a result, the N-terminal ends of H3 α2 and H4 α3 of the abutting H3-H4 heterodimers form the interface between two H3-H4 tetramers (Fig. 6B). This dislocation at the interface of two H3-H4 tetramers is responsible for the right-handedness of the CAF-1–bound ditetrasome, which sees an opening of ~45 Å between the two gyres of DNA situated diametrically from the tetramer-tetramer interface (Fig. 6A). The peculiar H3-H4 tetramer interface is stabilized by the binding of p60 to the nearby C-terminal portion of H4 α2 by means of the β propeller's ventral surface edge span-

ning blades 2 and 3 (Fig. 6C). Additionally, p60 is stabilized on DNA through a positively charged surface area adjacent to its H4 binding region, spanning the contiguous ventral surface edge of blades 3 and 4. The DNA binding property of p60 was confirmed by an electrophoretic mobility shift assay (EMSA) (fig. S13A). Furthermore, the αN helices of two centrally located H3s belonging to different H3-H4 tetramers became ordered and interacted with DNA, H4 α1 of the same heterodimer, and H4 α2 from the nonadjacent heterodimer of the other H3-H4 tetramer (fig. S13B). The right-handed ditetrasome does not permit continuous addition
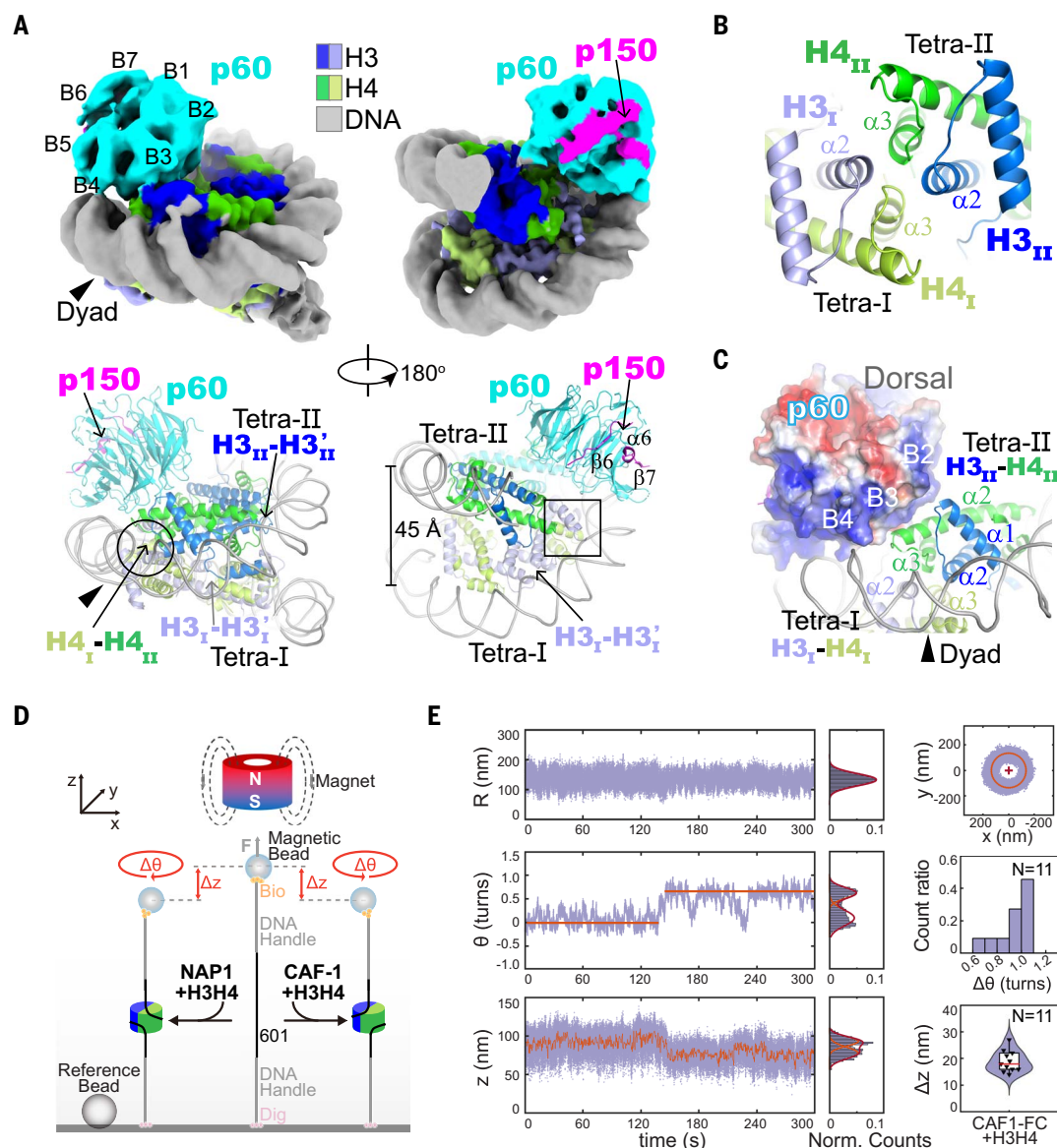
Fig. 6. CAF-1 induces right-handed DNA wrapping of H3-H4 in vitro.
(**A**) Two views of the 3.8-Å resolution cryo-EM structure of the CAF-1–bound right-handed ditetrasome. Shown at the top is a cryo-EM density map contoured at 3.0σ. Regions for H3, H4, and DNA are colored according to the displayed color stripes, whereas that of p60 and p150 are colored as in Fig. 2A. Blades 1 to 7 of p60 are labeled as B1 to B7. A black arrowhead marks the dyad position at the interface between two H3-H4 tetramers, Tetra-I and Tetra-II. Shown at the bottom is a cartoon model of the structure. The two H3-H3 interfaces within the two tetramers and the H4 interface between Tetra-I and Tetra-II, which is highlighted in a circle, are labeled with arrows. The box in the right panel indicates the location of ordered αN of H3 in Tetra-I interacting with H4 of Tetra-II. (**B**) A close-up view of the inter-tetrasomal interface corresponding to the encircled region in (A). (**C**) Interaction of p60 with one H3-H4 heterodimer and DNA at the inter-tetrasomal interface. The electrostatic potential surface of p60 (−3 to +3 k_BT/e) is shown. The positively charged region spanning blades 2 to 4 contacts histones and DNA. (**D**) Schematic of the single-molecule FOMT for determining the handedness of DNA wrapping. The clockwise and counterclockwise circular arrows represent left- and right-handed turns from views looking down at the beads. (**E**) The top row shows the time

course of radial fluctuation (left) based on the position of the bead (x, y) (right) and normalized counts of the left panel with Gaussian fit (middle) of a single DNA tether over a time span of 300 s covering an assembly event signified by simultaneous changes of bead rotation angle θ and extension length z shown below. The red circle in the right panel denotes the fitted overall circular motion of the bead. The middle row shows the time course of the bead rotation angle θ (left) and normalized distribution of θ changes with Gaussian fit (middle) of a single event. Mean values of each assembly step are indicated with red line segments. The histogram in the right panel shows the distribution of rotational changes (Δθ) from 11 independent tetrasome assembly events. The count ratio is defined as the number of times that a specific size rotation was observed divided by the 11 total events (N = 11). The bottom row shows the time course of the extension length (z) of a single DNA tether (left), with the red line showing z values averaged over 50-ms intervals, and normalized counts shown in the left panel with Gaussian fit (middle) of the same event as described above. The right panel shows the distribution of Δz values from the same 11 independent events as above displayed as a violin and box plot. The horizontal line represents the median, the height of the box extends the quartiles, and the whisker indicates the data range.

of H3-H4 tetramers because of steric clashes. Hence, discrete particles of ditetrasomes will be assembled on a long DNA. The extra density bound to p60 is consistent with being the β6-α6-β7 cassette of p150 CTR, which occupies the same location as p60 in the apo CAF-1 crystal structure and in the structure of CAF-1 bound to H3-H4; however, the rest of p150 and the entire p48 are missing (Fig. 6A). This observation suggests sizable conformational changes of CAF-1 upon deposition of H3-H4 onto DNA. A 5.6-Å resolution cryo-EM density map from the peak 2 sample shows the presence of two chunks of density clinging to the right-handed ditetrasome (fig. S10 and table S2), suggesting symmetric positioning of two p60-p150 units on both sides of the right-handed ditetrasome surface (fig. S10E). Finally, another distinct class of particles from peak 2 has a bigger lump of density bound to one side of a right-handed ditetrasome, resembling the presence of both p48 and p60 WD40 domains, but the low resolution of the map prevents further details from being elucidated (fig. S10C).

A nucleosome assembly intermediate, termed chromatin precursor, that consists of CAF-1, replicated DNA, and H3-H4 was previously predicted (8). It is surprising that we find a CAF-1–bound right-handed DNA ditetrasome in our in vitro assembly by salt dialysis. To exclude the possibility of an artifact from salt dialysis, we used a single-molecule freely orbiting magnetic tweezer (FOMT) method to investigate the handedness of DNA wrapping at a salt concentration of 50 mM KCl. Our experimental setup, analogous to that described in Vlijm *et al.* (54), is schematically shown in Fig. 6D. Observation of 11 independent assembly events shows that CAF-1 promoted right-handed DNA wrapping by an average of 0.9 turns, concomitant with the reduction of the DNA extension length by an average of ~19 nm (Fig. 6E and fig. S14A). By contrast, yeast NAP1 promotes left-handed DNA wrapping by an average of –0.9 turns, accompanied by the reduction of DNA extension of ~21 nm (fig. S14B). The latter result is consistent with a previous finding that NAP1-assembled tetrasomes are preferentially in a left-handed state, despite being able to spontaneously flip between the two handedness states (54). We cannot clearly distinguish whether DNA wraps one or two H3-H4 tetramers because the distribution of DNA extension change is quite broad, possibly indicating the existence of a mixture of tetrasomes and ditetrasomes.

Discussion

Our crystallographic and cryo-EM studies here reveal the long-anticipated structures of CAF-1 in the absence and presence of histones H3-H4. The structures uncover substantial structural plasticity and conformational dynamics

underlying CAF-1's histone binding activity, and our biochemical, nucleosome assembly, and transcriptional analyses corroborate the structural findings that the ED domain of p150 is crucial for H3-H4 binding. The structure of the 1:1 complex of CAF-1 and H3-H4 shows that the homodimerization interface of H3 is exposed, but formation of an H3-H4 tetramer is prohibited because of steric clashes with p60. This finding agrees with and provides structural rationales to the recent results from biochemical analyses of the yeast complex (35, 52).

Maintaining the integrity of parental and nascent H3-H4 tetramers during DNA replication has important implications in epigenetic inheritance (4). Our observation that the ED domain of p150 binds the large H3-H4 region that overlaps with the MCM2 binding site suggests a measure to segregate parental and newly synthesized H3-H4 (40). Assembly of H3-H4 tetramers from newly synthesized histones by CAF-1 is needed for proper chromatin inheritance. Interestingly, we found that the two H3-H4 heterodimers bound by two CAF-1 complexes are not in a tetrameric configuration, indicating that the process of H3-H4 tetramer assembly may be regulated. Although the structure of the 2:2 complex was only determined at relatively low resolution, the model was reliably built with the help of the higher-resolution 1:1 complex structure. In the 2:2 complex, the two H3-H4 heterodimers are positioned with the H3 dimerization interfaces next to each other, but their relative orientation and the distance between them deviate from that in an H3-H4 tetramer. It should be cautioned that our observation of the two H3-H4 dimers in the 2:2 complex does not exclude the possibility of a complex of CAF-1 with a H3-H4 tetramer that is not observed owing to low abundance or other conditions. For example, what we observed may represent a stable intermediate trapped under a specific condition, such as the DNA length used. In this arrangement, the spatial locations of the two p60s are the primary obstacle for aligning the two H3-H4 dimers for tetramer formation. Therefore, a remodeling of the interaction between p60 and H3-H4 is required for the assembly of an H3-H4 tetramer. It is possible that the binding of suitable-length DNA may facilitate efficient remodeling of the interaction between p60 and H3-H4 and the assembly of H3-H4 tetramers. Our SEC-MALS analysis showed that 30-bp DNA promoted the dimerization of two CAF-1–H3-H4 complexes, though the short DNA may have trapped the complexes at an intermediate state before the completion of the H3-H4 tetramer formation. Furthermore, a recent study also showed that DNA-loaded PCNA interacts with two CAF-1 complexes and promotes efficient nucleosome assembly (55).

Nucleosome assembly by CAF-1 occurs in two sequential steps: the formation of an H3-H4 tetrasome followed by the joining of H2A-H2B (8). Using the 147-bp Widom 601 DNA, we observed two different forms of ditetrasomes— a left-handed one and a CAF-1–bound right-handed one—from our in vitro assembly with H3-H4, DNA, and CAF-1. Considering that the left-handed ditetrasome was also obtained from the assembly of H3-H4 and DNA without CAF-1 (53), it most likely resulted from excessive H3-H4 added in our sample preparation. Handedness aside, the first critical question is whether ditetrasomes do occur during nucleosome assembly. Because histones H3-H4 are in a tetrameric form in the nucleosome, it has been taken for granted that the nucleosome assembly proceeds through an intermediate composed of a tetramer of H3-H4 wrapped by DNA. With a relatively short fragment of DNA (~80 bp), a well-defined complex of an H3-H4 tetramer with DNA can be identified in vitro (35, 56). However, when presented with a longer DNA, the distinction between two independent H3-H4 tetrasomes or a ditetrasome is unclear. It also remains to be determined whether ditetrasomes, as a transient intermediate or as a relatively stable form of a non-nucleosomal histone-DNA complex, occur in a physiological setting. Nevertheless, one may imagine certain advantages of proceeding through a ditetrasome intermediate during nucleosome assembly. For example, a ditetrasome may serve as a more authentic "placeholder" for nucleosomes because it engages more than 100 to 120 bp of DNA instead of the ~45 to 55 bp for a tetrasome.

It is surprising that DNA wraps H3-H4 tetramers in a right-handed form in the CAF-1–bound ditetrasome. A previous study showed that CAF-1 is associated with the chromatin precursor (8), but the exact form of the precursor is unknown. Biophysical and biochemical studies demonstrated that H3-H4 tetrasomes exist in a dynamic equilibrium of left-handed and right-handed forms in vitro (54, 57). However, very little is known about the right-handed DNA wrapping of histones in physiological settings, except in the context of centromeric chromatin (58). The structure of the CAF-1–bound right-handed ditetrasome and our single-molecule FOMT characterizations demonstrate that CAF-1 promotes right-handed DNA wrapping in vitro. Whether this also occurs in vivo and what the functional implication might be are not presently clear. We may speculate that a right-handed intermediate may balance the predominantly left-handed torsion of the tetrasome assembled from parental H3.1-H4, which are inherited mostly as an intact tetramer (4), to alleviate torsion stress and facilitate timely progression of the replication fork. It may also be helpful for replication of certain specialized chromosomal regions such as the centromere. Clearly, future efforts are needed to validate

and characterize the physiological roles of right-handed DNA wrapping by CAF-1.

Materials and methods

Plasmid construction

Recombinant CAF-1 subunits were produced in insect cells using baculoviruses prepared from modified vectors of pFastBac1 (Invitrogen). Plasmids carrying an N-terminal fusion of GST to p150 and a C-terminal fusion of 6×His tag to p60 and p48 were constructed by standard methods. A PreScission protease cleavage site was engineered between the GST tag and the p150 fragment. For large-scale production of full-length CAF-1 for structural and functional analyses, cDNA of full-length human p150 was subcloned into a modified pMlink vector containing N-terminal Protein A tag, and cDNAs for p60 and p48 were subcloned into pMlink vector without tags. A PreScission protease cleavage site was engineered between the Protein A tag and the p150 gene. Production of full-length human histones H3.1 and H4 in bacteria was performed using a bicistronic plasmid constructed with the pCDFDuet1 vector (Novagen). Truncation variants or point mutants of p150 and p60 and histones H3.1 or H4 were generated with the KOD-Plus-Mutagenesis kit (TOYOBO, SMK-101) following the manufacturer's protocols. All constructs were verified by DNA sequencing.

To convert the original AID system to AID2 (*44*), a point mutation was introduced into the OsTIR1 cDNA sequence in pMK232 (CMV-OsTIR1-PURO, Addgene, no. 72834). The OsTIR1(F74G) cDNA sequence was cloned into AAVS1-Neo-CAG-Flpe-ERT2 (Addgene, no. 68460) by Seamless Cloning (Beyotime) to replace the Flpe-ERT2 sequence. The spacer sequence targeting *AAVS1* was cloned into lentiCRISPRv2 (Addgene, no. 52961) following the instructions by the inventors. An AID-P2A-PuroR-tag was knocked-in immediately before the stop codon of *p150* or *p60* by CRISPR-Cas9–mediated homologous recombination. The construction of the repair template donor plasmid for the *p150*-AID knock-in was described previously (*59*), and the donor plasmid for the *p60*-AID knock-in was constructed accordingly. The spacer sequences targeting *p150* and *p60* were cloned into lentiCRISPRv2. For the p150 and p60 rescue experiments, full-length *p150* or *p60* cDNA was cloned into pCW-Cas9 (Addgene, no. 50661) by Seamless Cloning to replace the original spCas9 sequence, and blasticidin resistance was generated by replacing PuroR with blasticidin S deaminase sequence, which was subcloned from plasmid lenti dCAS-VP64_Blast (Addgene, no. 61425). p150 and p60 mutant constructs were generated by mutagenesis polymerase chain reaction (PCR).

Protein expression and purification

CAF-1 proteins were expressed in Sf21 cells using the Bac-to-Bac baculovirus expression system (Invitrogen). WT or various mutant CAF-1 complexes were produced by suspension cell culture coinfected with recombinant baculoviruses for each subunit following the manufacture's protocol. The full-length CAF-1 complex was also expressed using human embryonic kidney 293F (HEK293F) cells. A total of 500 ml of HEK293F cells was transfected with 0.5 mg of plasmids of three CAF-1 subunits (1:1:1 molar ratio) plus 2 mg of linear polyethylenimine. The cell culture was harvested 48 hours after transfection at 37°C.

The expressed CAF-1 middle domain complex (CAF1-MC) contains GST-tagged p150M (residues 442 to 714), p60ΔC-His, and p48-His, and the complex was purified first by resuspension of cell pellets in five volumes of the lysis buffer containing 20 mM Tris-HCl, pH 7.5, 500 mM NaCl, 5 mM imidazole, 1 mM phenyl-methylsulphonyl fluoride (PMSF) and the protease inhibitor cocktail, before lysis by sonication. Cell debris was removed by centrifugation, and the cleared supernatant was incubated with Ni-NTA agarose resins for 30 min at 4°C, followed by washing the resins three times with the lysis buffer. The bound proteins were eluted with 500 mM imidazole in the lysis buffer. Immediately following the elution, 1 mM each of EDTA and dithiothreitol (DTT) were added to the Ni-NTA eluate, which was then incubated with glutathione (GSH) sepharose resins (GE Healthcare) preequilibrated in buffer A-500 (20 mM Tris-HCl, pH 7.5, 500 mM NaCl, 1 mM EDTA, and 1 mM DTT) for 2 hours. The loaded GSH resins were washed three times with buffer A-500, followed by elution of the bound proteins with the addition of 30 mM GSH. The GST-tag was cleaved by PreScission protease during dialysis to 100 mM NaCl overnight, and the sample was further purified on a Q column (GE Healthcare) with a linear 0.1 to 2 M NaCl gradient. Eluted fractions were analyzed by SDS–polyacrylamide gel electrophoresis (SDS-PAGE), and those highly enriched with CAF1-MC were pooled and concentrated and loaded onto a HiLoad 16/60 Superdex 200 column (GE Healthcare) in buffer A-500. Elution fractions containing highly purified CAF1-MC were pooled and concentrated to ~20 mg/ml by ultrafiltration and stored at −80°C before use.

The larger CAF-1 complex (CAF1-LC) containing the p150L (residues 442-853) fragment, which includes the WHD domain, was purified following a similar procedure, except that the ion-exchange column chromatography step was omitted. Full-length CAF-1 complex (CAF1-FC) supernatant was incubated with immunoglobulin G (IgG) beads for 2 hours, and unbound proteins were extensively washed away with buffer A-500. The fusion proteins were digested using PreScission protease overnight to remove tags, and the complex was eluted with buffer A-500. The eluted proteins were further purified using a Superose 6 increase 10/300 GL (GE Healthcare) size-exclusion column in buffer A-2000, which contains 2 M NaCl. C-terminal 6×His-tagged p48 and p60ΔC proteins were purified through successive Ni-NTA, respective ion-exchanges with Q and Heparin columns, and HiLoad 16/60 Superdex 200 sizing column steps.

WT and mutant human histone H3.1-H4 complexes were coexpressed using the pCDFDuet1-H3.1-H4 plasmid in *Escherichia coli* BL21 CodonPlus (DE3) RIL cells. Protein production was induced with 0.5 mM isopropyl-β-D-thiogalactopyranoside (IPTG) at 37°C for 4 hours. Histone complexes were first purified through a 5-ml SP column (GE Healthcare), followed by purification through a gel-filtration column at 2 M NaCl.

Crystallization

Initial small and thin-plate-shaped crystal clusters of the CAF1-MC complex were grown by sitting-drop vapor-diffusion at 20°C with 1.0 µl of protein solution (7 to 10 mg/ml) mixed with 1.0 µl of reservoir solution containing 8% (v/v) Tacsimate, pH 6.0, and 20% (w/v) PEG 3350. Multiple rounds of crystallization condition optimization yielded larger crystals in the reservoir solution containing 7% Tacsimate, pH 6.0, 22% (w/v) PEG 3350, 0.12 M lithium citrate, and 0.05 M sodium tartrate by hanging-drop vapor-diffusion at 4°C. Streak-seeding of previous optimized crystals into a protein-reservoir solution mixture at half of the protein concentration (3 to 5 mg/ml) preincubated overnight against reservoir solutions with 15 to 25% (w/v) PEG3350 and 0 to 0.2 M sodium tartrate was used to further improve the crystal quality. Single, thick crystals were obtained in a condition with 7% Tacsimate, pH 6.0, 18% (w/v) PEG 3350, 0.12 M lithium citrate, and 0.13 M sodium tartrate after 3 to 5 days. Cryogenic data collection was performed with cryoprotectants prepared by supplementing the crystallization mother liquor with 15% glycerol.

X-ray diffraction data collection, structure determination, and refinement

Diffraction data were collected at the Shanghai Synchrotron Radiation Facility (SSRF) beamline BL17U equipped with a Quantum 315r CCD detector (ADSC) using a wavelength of 0.97915 Å or beamline BL19U using Pilatus 6M detector at a wavelength of 0.97853 Å. Data were processed using the HKL2000 software package (*60*). Most of the crystals belong to the C222₁ space group, whereas a small percentage have a P2₁ or a C2 space group. The C222₁, P2₁, and C2 crystals diffracted to 3.5-, 3.6-, and 3.4-Å resolutions, respectively. The C222₁ structure was determined by molecular replacement (MR) with PHASER (*61*) using the crystal structures of human p48/RBBP4 [Protein Data Bank (PDB) ID 3GFC] and the human WD40-repeat protein Ciao1 (PDB ID 3FM0) as the search models.

Refinement of the MR solution gave rise to unambiguous extra densities attributable to p150 near p48 and p60. An initial model of CAF1-MC was manually built with COOT (*62*), and the model was improved by iterative cycles of refinement with PHENIX (*63*) and model adjustment. The refined model has R_{work} and R_{free} values of 0.225 and 0.257, respectively, and good stereochemical quality, with 96.8 and 3.2% of the residues in the favored and allowed regions of Ramachandran plot, respectively. The ordered structure contains residues 463 to 713 of p150, residues 1 to 394 of p60, and residues 7 to 411 of p48. Internal disordered segments of p150 spanning residues 607 to 657, which is highly enriched with acidic residues, and residues 100 to 111 of p60 are not included in the final model. The structures from the other two crystal forms were subsequently solved by molecular replacement using the $C222_1$ structure as a search model. Finally, the models were validated with MolProbity (*64*). Detailed statistics for data collection and structure refinement are shown in table S1.

DNA preparation

A 30-bp double-stranded DNA fragment (DNA_{30}) was prepared by annealing two high-performance liquid chromatography (HPLC)–grade chemically synthesized complementary DNA strands (forward: 5′-GTAATCCCCTTGGCGGTTAAAACGCGGGGG-3′; and reverse: 5′-CCCCCGCGTTTTAACCGCCAAGGGGATTAC-3′) in the annealing buffer (10 mM HEPES, pH 7.5, 100 mM NaCl, and 5 mM $MgCl_2$) at a concentration of 20 μM by ramping temperature down from 95° to 4°C at a rate of 0.1°C/s.

The 147-bp Widom 601 (W601) DNA was produced in *E. coli* following a published procedure (*65*, *66*). Briefly, tandem copies of the 147-bp W601 DNA fragment were inserted into a pEGFP-N1 vector (Addgene), and recombinant plasmids were produced in large bacterial culture. The 147-bp DNA was excised from the plasmid by EcoRV digestion, isolated by polyethylene glycol (PEG) precipitation, and further purified through ethanol precipitation. The sequence of the 147-bp W601 DNA is 5′-CTGGAGAATCCCGGTGCCGAGGCCGCTCAATTGGTCGTAGACAGCTCTAGCACCGCTTAAACGCACGTACGCGCTGTCCCCCGCGTTTTAACCGCCAAGGGGATTACTCCCTAGTCTCCAGGCACGTGTCACATATATACATCCTGT-3′.

Cryo-EM sample preparation

The CAF-1 complex with the p150L fragment encompassing the WHD domain (CAF1-LC) and histones H3-H4 were mixed at a 1:2.5 molar ratio in buffer A-500, followed by incubation on ice for 30 min, purification through a HiLoad 16/60 Superdex 200 column to remove excessive histones, and concentration of the purified complex to ~10 mg/ml. The preassembled CAF1-LC–H3-H4 complex and DNA_{30} were then mixed

at a molar ratio of 1:1.5 in buffer A-500, and then dialyzed to buffer B (20 mM HEPES, pH 7.5, 50 mM NaCl, and 1 mM DTT) at 4°C for 36 hours. Preparation of the CAF1-FC–H3-H4–DNA30 complex is similar to that of the CAF1-LC complex, except that a Superose 6 increase 10/300 GL column (GE Healthcare) is used for the sizing column.

Preparation of the complexes of CAF-1, H3-H4, and W601 DNA (DNA_{147}) was performed by mixing WT or truncation variants of CAF-1, histones H3-H4, and DNA_{147} at a 1:2.5:1 molar ratio in buffer A-2000 and dialyzed to buffer B at 4°C in 36 hours.

The four samples above, with concentrations at ~1 mg/ml and a volume of 200 μl each, were subjected to glutaraldehyde cross-linking during GraFix (*67*). Specifically, the sample was subjected to a 12-ml linear 10 to 30% glycerol gradient in buffer B supplemented with 0 to 0.15% EM-grade glutaraldehyde (Sigma-Aldrich). After centrifugation at 4°C for 16 hours at 38,000 rpm in an SW40 rotor (Beckman Coulter), the sample was manually fractionated into 25 aliquots of 500 μl each from top to bottom using pipettes. The fractions were analyzed on an 8% denaturing polyacrylamide gel, and cross-linked fractions were further examined by negative-staining EM for particle homogeneity.

Suitable fractions were dialyzed to buffer A-50, which is identical to A-500 except that the NaCl concentration is changed to 50 mM, and cryo-EM specimens were prepared using the 300 mesh R2/1 CryoMatrix/Amorphous alloy film grid (Zhenjiang Lehua Technology Co, Ltd.) for the CAF1-LC–H3-H4–DNA_{30}, CAF1-FC–H3-H4–DNA_{30}, and CAF1-LC–H3-H4–DNA_{147} samples and the 300 mesh Quantifoil R2/1 gold grid for the CAF1-LC–H3-H4–DNA_{147} sample. The grids were treated with the Gatan Model 950 Advanced Plasma system using O_2/Ar for 60 s. A 3-μl aliquot of the sample at a concentration of ~0.4 mg/ml was applied to glow-discharged grids. After incubation for 10 s, excess sample was blotted with filter paper (diameter 55 mm, Whatman, GE Healthcare) for 3 to 4.5 s, and the grid was flash-frozen in liquid ethane using a FEI Vitrobot Mark VI device (ThermoFisher). All cryo-EM samples were prepared at 10°C and 100% relative humidity.

Cryo-EM data acquisition, image processing, and 3D reconstruction

Cryo-EM images were collected on an FEI Talos Arctica electron microscope equipped with a GIF Quantum energy filter and operating at 200 kV with a nominal magnification of 130,000. Images were recorded by a Gatan Bio-Quantum K2 Summit direct electron detector. The slit width for zero-loss peak was 20 eV. The camera was in a super-resolution mode with a 1-Å physical pixel size (0.5-Å super-resolution pixel size). The defocus range was set between –1.0 and –1.5 μm. Each image was exposed for 5 s, resulting in total electron exposure of ~50 e$^-$/Å^2

(exposure rate, 8.9 e$^-$/pixel/s) and 32 frames per movie stack.

A summary flow chart of data processing and structure determination procedures for the dataset obtained with the CAF1-LC–H3-H4 complex and DNA_{30} is shown in fig. S3. A total of 23,996 movies were collected and imported into cryoSPARC (*68*) and aligned using patch-based motion correction, and contrast transfer function (CTF) parameters were estimated in a patch manner using cryoSPARC and Gctf (*69*). Micrographs with poor Thon ring or heavy contamination were removed in the screening, and 19,607 micrographs were selected for further data processing. Particles of the complex were initially picked with cryoSPARC reference-free blob picker and used to generate 2D references for template-based auto-picking. Together with deep picking via topaz in cryoSPARC, a total of 19,430,612 particles were obtained. The dataset was cleaned up by several rounds of 2D classification, and 2,269,295 particles were kept for ab initio model generation (two classes) and subsequent heterogeneous refinement. These procedures resulted in two highly populated classes, monomeric and dimeric CAF1-LC–H3-H4 complexes. A new round of ab initio model generation (three classes for the monomer dataset and two for the dimer dataset), heterogeneous refinement, and nonuniform refinement on each class were performed to clean up the monomer and dimer datasets. For the monomer dataset, 927,863 particles in the best class were imported to Relion-3.0 (*70*) using the csparc2star.py script in pyem (*71*) and further sorted into four classes by 3D classification. The best class containing 400,801 particles was selected and further sorted into eight classes by no-alignment 3D classification. Three top classes were combined, and a total of 304,368 selected particles were subjected to cryoSPARC for nonuniform refinement, yielding a 3.9-Å map. Local refinement with a local mask improved the map resolution to 3.8 Å. For the dimer dataset, 53,708 particles were transferred to Relion-3.0 for 3D classification into four classes, and 24,904 particles in two classes were selected and subjected to nonuniform refinement, yielding a map with an overall resolution of 7.2 Å for the CAF1-LC–H3-H4 dimeric complex. Further refinement with C2 symmetry resulted in a 6.1-Å resolution map.

For the CAF1-FC–H3-H4–DNA_{30} dataset, as shown in fig. S4, a total of 15,893 movies were collected and imported into cryoSPARC and aligned using patch-based motion correction, and CTF parameters were estimated in a patch manner using cryoSPARC. Micrographs with poor Thon ring or heavy contamination were removed in the screening, and 14,532 micrographs were selected. The particles were picked with cryoSPARC reference-free blob picker initially and were used to generate 2D references for template-based autopicking. A total of 4,999,183

particles were autopicked using template and topaz. Several rounds of 2D classification were performed to clean up the dataset, and a total of 1,199,544 particles were kept for ab initio model generation and heterogeneous refinement using six classes. The best class with 688,535 particles was selected for nonuniform refinement, yielding a 3.6-Å map. Because the CAF1-FC–H3-H4 map is similar to that of CAF1-LC–H3-H4 (correlation value 0.976), particles in these two datasets were combined and overlaps were removed (within radius of 130 Å) to generate a combined set of 977,978 particles. Ab initio model generation and heterogeneous refinement using six classes resulted in two highly populated classes: monomers and dimers of CAF-1–H3-H4. The best two classes of the CAF-1–H3-H4 monomer containing 552,289 particles were selected and subjected to a further round of ab initio model generation and heterogeneous refinement using six classes. The best four classes containing 530,555 particles were selected for nonuniform refinement. Local refinement with a local mask improved the map resolution to 3.5 Å. In the final monomer particle set, 77 and 23% of the particles are from the FC and LC particle sets, respectively. The CAF1-FC dimer class containing 168,932 particles was combined with the CAF1-LC dimer dataset containing 53,708 particles, and the overlap removed within the 130-Å radius. A total of 197,148 particles were kept for ab initio model generation and heterogeneous refinement using six classes, and 50,508 particles in the best class were selected and subjected to nonuniform refinement, yielding a structure of the CAF-1–H3-H4 dimer at an overall resolution of 6.3 Å. Further refinement using C2 symmetry produced a 5.9-Å map of the dimeric CAF-1–H3-H4 complexes. Symmetry expanding to C1 generated 101,016 particles, and local refinements were performed by applying two local masks covering the two protomers, yielding two maps at 4.63-Å (protomer I) and 4.58-Å (protomer II) resolution. The composite map used for model building, refinement, and deposition was generated by aligning and merging the two locally refined maps using the Combine-Focused-Maps module in PHENIX. The half-maps of each local refined protomer were also merged and used for overall Fourier shell correlation (FSC) calculation in cryoSPARC, resulting in a 4.6-Å resolution composite map of the dimeric CAF-1–H3-H4 complex.

A summary flow chart of data processing and structure determination procedures for the peak 1 dataset of the CAF1-LC–H3-H4–DNA$_{147}$ complex is shown in fig. S9. Data pre-processing steps were similar to those used with the 30-bp DNA oligomer. From this, 11,206 movies were collected and 10,316 micrographs were selected for particle picking after patch motion correction and patch CTF estimation by cryoSPARC. Because of the relatively small size of the pro-

tein complex, it is difficult to distinguish particles of the intact protein complex or partial complexes, and a large set of particles, 10,865,604 in total, were initially picked and extracted. The dataset was cleaned up through several rounds of 2D classification, and a total of 1,088,125 particles were kept for ab initio model generation and heterogeneous refinement. Two highly populated classes were obtained: one is a left-handed ditetrasome, and the other is the CAF-1–bound right-handed ditetrasome. These two subsets of data were imported to Relion-3.0 for further 3D classification.

For the left-handed ditetrasome subset of data, 459,354 particles were sorted into four classes by 3D classification. Three top classes were combined, and a total of 335,568 particles were selected for nonuniform refinement, which yielded a map at an overall resolution of 3.5 Å. For the CAF-1–bound right-handed ditetrasome subset of data, 628,771 particles were sorted into six classes by 3D classification. Two top classes containing 178,734 particles were combined and subjected to nonuniform refinement, yielding a map at an overall resolution of 3.8 Å.

Figure S10 summarizes data processing and structure determination procedures for the dataset collected from the peak 2 sample. From this, 2213 movies were collected, and 2007 micrographs were kept for particle picking. A large set of 1,568,202 particles were initially picked and extracted. A total of 243,993 particles were kept after multiple rounds of 2D classification and used for ab initio model generation and heterogeneous refinement. Three classes of particles were obtained, and the 126,187 particles in the best class were imported to Relion-3.0 for 3D classification and resulted in six classes. One class containing 8190 particles showed two extra chunks of density on one side of the ditetrasome surface, with a low resolution of ~18 Å. Two other classes both have one extra piece of density on each side of the ditetrasome surface, and the better class containing 76,910 particles was selected and subjected to nonuniform refinement, yielding a map of two CAF-1–bound ditetrasomes at an overall resolution of 5.6Å and 6.3 Å with and without C2 symmetry imposed, respectively.

A flow chart summarizing data processing procedures for the CAF1-FC–H3-H4–DNA$_{147}$ complex is shown in fig. S11. From this, 8801 movies were collected, and 8002 micrographs were kept for particle picking. A large set of 3,199,346 particles were initially picked and extracted. A total of 947,480 particles were kept after multiple rounds of 2D classification and used for ab initio model generation and heterogeneous refinement with six classes. The 104,027 particles in the best class were further used for the next round of ab initio model generation and heterogeneous refinement by six classes. These procedures resulted in two highly populated classes: single and double CAF1-FC–ditetrasome com-

plexes. For the single CAF1-FC–ditetrasome, two classes containing 67,319 particles were subjected to nonuniform refinement, yielding a map of single CAF-1–bound ditetrasome at an overall resolution of 3.8 Å. The 13,993 particles of the double CAF1-FC–ditetrasome class were used for nonuniform refinement, yielding a map of the double CAF-1–bound ditetrasome at an overall resolution of 6.6 Å.

All reported resolutions were estimated based on the gold-standard FSC criterion of 0.143. Local resolutions were estimated by cryoSPARC.

Model building and refinement of the cryo-EM structures

Crystal structures of CAF1-MC from this study and the histone H3.1-H4 model from the sNASP–ASF1–H3.1-H4 complex (PDB ID 7V6Q) were used as initial models for building the model of the CAF1-LC–H3-H4 complex by docking each component into the cryo-EM map in UCSF Chimera (72). The resulting 1:1 model of the CAF1-LC–H3-H4 complex was used as the initial model for fitting the structure of the 2:2 complex. For the left-handed ditetrasome structure, the atomic models of the Widom 601 DNA (PDB ID 3LZ0) and the histone H3.1-H4 heterodimer were fitted into the cryo-EM map. For the CAF-1–bound ditetrasome, the crystal structure CAF1-MC from this study and histones H3.1-H4 were fitted into the map, and the right-handed Widom 601 DNA model was built manually. An additional CAF1-MC complex was introduced into the model of the right-handed ditetrasome bound by two CAF-1 complexes.

The final models were obtained after iterative cycles of real-space refinement using PHENIX with secondary structure and Ramachandran and rotamer restraints, assisted with manual editing, adjustment and model rebuilding in COOT. Three macro cycles of final refinement were performed with the minimization_global and local_grid_search strategies, and the qualities of the refined models were checked with the MolProbity parameters calculated using PHENIX. For the four low-resolution structures, the 4.6- and the 6.1-Å dimeric CAF-1–H3-H4 complexes and the 5.6- and the 6.6-Å double CAF-1–bound ditetrasome complexes, only main chains were kept in these models. These models were real-space refined using PHENIX as rigid bodies with secondary structure and Ramachandran restraints. Also, in the two 3.8-Å single CAF-1–ditetrasome complexes, only the main-chain model for p60 and p150 were kept because of the limit of local resolutions. The final refinement statistics are shown in tables S2 and S3. Structural figures were prepared using Chimera, ChimeraX (73), and PyMOL (Schrödinger LLC, New York, NY).

Topological assay for nucleosome assembly

DNA supercoiling assays were performed as described previously (74) with the following

modifications. Relaxed DNA template was prepared by combining φX174 RF I DNA (NEB, N3021S) at 100 ng per sample, with excess DNA Topoisomerase I (TaKaRa, 2240A) in the assembly buffer [10 mM Tris-HCl, pH 7.5, 125 mM NaCl, 2 mM MgCl₂, 0.5 mM DTT, and 0.1 mg/ml bovine serum albumin (BSA)] at 37°C for 1 hour and kept at room temperature ready for use. Histones H3.1-H4 (100 ng) were preincubated with 100 and 200 ng each of yNAP1, WT CAF-1, or its mutants in the assembly buffer at 37°C for 30 min. To initiate the assembly reaction, 100 ng of relaxed plasmid DNA was added to the chaperone-histone mixture and incubated for 15 min at 37°C. The 25-μl standard chromatin assembly reaction was stopped by the addition of EDTA to 20 mM and SDS to 0.5% and 0.5 mg/ml proteinase K, followed by incubation at 55°C for 15 min before phenol-chloroform extraction. The DNA samples were analyzed on a 1% agarose gel in 1× TAE buffer (40 mM Tris-acetate, 1 mM EDTA) at 90 V for 4 hours with ethidium bromide staining.

GST-pulldown

To analyze the interaction of p150 with p48 and p60ΔC proteins, 3 μg of GST or GST-fused p150M or different p150 fragments were first immobilized on 5 μl of glutathione Sepharose 4B resins (GE Healthcare), followed by incubation with 5 μg each of p48 and p60ΔC in 500 μl of binding buffer (20 mM Tris-HCl, pH 7.5, 500 mM NaCl, 5 mM 2-mercaptoethanol, and 1 mM EDTA) under continuous rotation at 4°C for 2 hours. The resins were then washed five times with 1 ml of binding buffer. Bound proteins were eluted in the SDS sample buffer, separated on a 15% SDS-PAGE gel, and stained with Coomassie blue.

To test the interactions between CAF-1 and histones H3-H4, 3 μg of GST or GST-fused WT or mutant CAF-1 complexes were immobilized on 5 μl of glutathione Sepharose 4B resin (GE Healthcare), which was then mixed with 5 μg of H3.1-H4 or its mutants in 500 μl of binding buffer (20 mM Tris-HCl, pH 7.5, 500 mM NaCl, 5 mM 2-mercaptoethanol, 0.01% NP-40, and 1 mM EDTA), and the mixture was rotated overnight at 4°C. The resins were then washed five times with 1 ml of washing buffers modified from the binding buffer with 0.1% NP-40 and 500 mM or 1 M NaCl. Bound proteins were eluted in the SDS sample buffer and analyzed by Coomassie-stained SDS-PAGE.

Cell lines

HEK 293FT cells (Thermo Fisher, R70007) were maintained in Dulbecco's modified Eagle medium (DMEM) (Gibco) supplemented with 10% (v/v) fetal bovine serum (FBS) (Biological Industries) and penicillin-streptomycin (Sangon Biotech). HAP1 cells (Horizon) were cultured in Iscove's modified Dulbecco's medium (IMDM) (Gibco) supplemented with 10% FBS and penicillin-streptomycin. To integrate the OsTIR1 expres-

sion cassette into the *AAVS1* locus, cells cotransfected with AAVS1-Neo-CAG-OsTIR1(F74G) and lentiCRISPR-sgAAVS1 by jetOPTIMUS (Polyplus) were selected by 1 mg/ml G418 for 7 days and then seeded into 96-well plates by fluorescence-activated cell sorting (FACS). Clones from single cells were expanded and analyzed by Western blotting and reverse transcription quantitative PCR (RT-qPCR). AID-tagged *p150* or *p60* fusion clones were generated as previously described (75). Transfected cells were selected by 0.2 μg/ml puromycin for 2 days. Cell clones from single cells were expanded and analyzed by genotyping PCR and Western blotting. Only clones with biallelic insertions were kept for future experiments. Constructs expressing *p150* or *p60* were introduced into p150-AID or p60-AID cells by lentiviral transduction, respectively; stable cells were selected by 5 μg/ml blasticidin; and expressions of exogenously introduced genes were examined by Western blotting.

RNA-seq and data analysis

Cells grown in a six-well plate were extracted with 1 ml of TRIzol reagent (ThermoFisher, 15596026) according to the manufacturer's instructions. Total RNA was prepared with two biological replicates for each genotype or treatment. Poly-A–tailed mRNA molecules were captured using attached oligo-dT and subjected to library construction according to the manufacturer's recommendations.

mRNA-seq libraries were sequenced on the NovaSeq 6000 platform by Annoroad Gene Technology Co., Ltd., using STAR aligner (v2.7.9a), and mRNA-seq read pairs were mapped to the human genome sequences (hg38) with Gencode annotations. Differential gene expression analysis was performed using DESeq2 software, and differentially expressed genes (DEGs) were identified using the cutoff adjusted p value ≤0.05 and fold change ≥2.

Cell proliferation assays

To analyze the effects of p150 and p60 mutants on cellular proliferation, cells were seeded into 96-well plates at a density of 1000 cells per well. Doxycycline was added to the medium at a final concentration of 2 μg/ml while seeding. After 24 hours, the medium was changed, and 5-Ph-IAA was added to cells at a final concentration of 1 μM to induce the degradation of endogenous p150 or p60 in the presence of doxycycline to maintain the expression of exogenous p150 or p60. Medium was changed every day to supply fresh doxycycline and 5-Ph-IAA. At 6 days after 5-Ph-IAA treatment, cell viability was measured by CellTiter-Glo reagent (Promega). Survival rate was quantified as the ratio of the number of survived cells to the cell number in the control treatment.

ReIN-Map, MNase-seq, and data analysis

The ReIN-Map protocol was adapted and modified from those used in (76–78). To analyze the

effects of CHAF1A and CHAF1B mutants on nascent nucleosome landscape after DNA replication, cells were seeded into 150-mm dishes at a density of 1×10^7 per dish. Twelve hours after seeding, doxycycline was added to the medium at a final concentration of 2 μg/ml. After 24 hours, the medium was changed, and 5-Ph-IAA was added to a final concentration of 1 μM in the presence of doxycycline to maintain the expression of exogenous CHAF1A or CHAF1B. After 6 hours, the cells were pulse-labeled with 20 μM EdU (SANTA CRUZ, sc-284628) for 10 min. After the EdU pulsing, cells were immediately fixed in 1% formaldehyde for 10 min. Then, glycine was added to a final concentration of 0.125 M, and the reaction was incubated for 5 min at room temperature. Cells were then collected by scraping with a cell lifter and transferred into 15-ml tubes. After centrifugation, the cell pellets were resuspended in cold PBS and transferred into a 1.5-ml Eppendorf tube.

Fixed cells were resuspended in Buffer I (50 mM HEPES, pH 7.5, 1 mM EDTA, 140 mM NaCl, 10% glycerol, 0.5% NP-040, and 0.25% Trition X-100) and incubated at 4°C for 10 min. After centrifugation, the cell pellets were resuspended in Buffer II (10 mM Tris-HCl, pH 7.5, 1 mM EDTA, 0.5 mM EGTA, and 200 mM NaCl) and incubated at room temperature for 10 min. After centrifugation, cell nuclei were resuspended with Buffer III (10 mM Tris-HCl, pH 7.5, 60 mM KCl, 15 mM NaCl, and 3 mM MgCl₂), and briefly sonicated for 30 s with a bioruptor (Diagenode). The samples were split into two 1.5-ml Eppendorf tubes for MNase digestion and chromatin sonication separately. For MNase digestion, 300-μl samples were incubated at 37°C for 3 min with 10 μl of MNase (lab stock), and digested in the presence of 2 mM CaCl₂ for 10 min. The digestion was stopped with a final concentration of 10 mM EDTA, and SDS was added at a final concentration of 1%. For chromatin sonication, SDS was added at a final concentration of 1%, and 300-μl samples were transferred into a sonication tube. Then, 1 ml of NLB buffer (50 mM Tris, pH 7.5, 10 mM EDTA, and 1% SDS) and sonication beads were added to each sample and sheared to 300- to 500-bp-sized fragments with a bioruptor. Both MNase-treated and sonication-fragmented chromatin were de–cross-linked at 65°C overnight with 50 μg of proteinase K. After incubation, phenol-chloroform-isoamyl alcohol (PCI) extraction was performed, and RNase-A was added to the aqueous phase, which was then incubated at 37°C for 15 min. PCI extraction was performed again, and the DNA in the aqueous phase was precipitated by adding 2.5× volume of ethanol, 200 mM NaCl, and glycogen and then incubated at −20°C overnight. After centrifugation, the DNA pellet was washed with 70% ethanol and resuspended in 10 mM Tris-HCl, pH 7.5. The extracted DNA

fragments were subjected to end repair, A-tailing, and adaptor ligation using the NEB Ultra II DNA Library Prep kit (E7645) following the manufacturer's instructions. After reserving an aliquot for input (MNase-seq), EdU-pulsed DNA (MINCE-seq and Sonication-seq) was biotinylated under the following conditions: 15 mM Tris-HCl, pH 7.5, 0.5 mM biotin-TEG-azide (Jena Bioscience), 0.1 mM CuSO$_4$ (Sigma-Aldrich), 0.5 mM THPTA (Sigma-Aldrich), and 10 mM sodium ascorbate (Sigma-Aldrich) for 45 min at room temperature. DNA fragments were purified using AMPure XP beads (1.1×) and resuspended in 10 mM Tris-HCl, pH 7.5. Next, biotinylated DNA was pulled down using Myone C1 beads (Invitrogen). Six µl of beads per sample were balanced by three washes with 1× BW&T buffer (5 mM Tris-HCl pH 7.5, 0.5 mM EDTA, 1 M NaCl, and 0.05% Tween-20) and resuspended in 2× BW&T buffer. Streptavidin beads were then mixed 1:1 with biotinylated DNA and rotated for 45 min at room temperature. Then, the beads were washed four times with 1× BW&T, twice with 1× TE with 0.05% Tween-20, and once with 10 mM Tris-HCl, pH 7.5 and resuspended in 10 µl of ddH$_2$O. The beads were incubated at 98°C for 10 min, and 16 cycles of PCR amplification were performed together with input DNA libraries. Post-PCR clean-up was performed by adding 1× volume of AMPure XP beads. Two independent biological repeats were performed for each sample, and similar results were obtained for all analyses.

Pair-end sequencing reads were processed, and the samples were mapped to *Homo sapiens* genome (hg38) by Bowtie2 (*79*) using default parameters. Uniquely mapped reads were collected for further analysis. Nucleosome positions were called using the statistic pipeline DANPOS (*80*) with the fragments of size 120 to 180 bp. Mononucleosome coverage was smoothed with a 10-bp flat window. ReIN score is defined as the normalized read density of MINCE-seq divided by the density of Sonication-seq samples. MINCE-seq signals are influenced by both DNA synthesis and nucleosome assembly. Thus, by normalizing MINCE-seq with Sonication-seq, the nucleosome occupancy score reflects nucleosome occupancy independent of DNA synthesis and EdU incorporation. All profiles relative to a feature of TSSs or CTCF-binding sites were plotted as the ReIN score or nucleosome occupancy score spanning a given position relative to the feature over a ±1000-bp window around the feature midpoint. The CTCF chromatin immunoprecipitation sequencing (ChIP-seq) data are from the Gene Expression Omnibus (GEO) (GSM4640493) (*81*)

Molecular weight determination by SEC-MALS

Molar masses of protein or protein-DNA complexes in solution were determined by SEC-MALS using the DAWN HELEOS™ II 18-angle static light-scattering system (Wyatt Technology) connected to an Agilent HPLC that was hooked up with a Superose 6 increase 10/300 GL column (GE Healthcare). The system was first equilibrated in a buffer containing 20 mM Tris-HCl, pH 7.5, 125 mM NaCl, and 2% glycerol for 12 hours. The equilibrated system was then calibrated with BSA at a concentration of 1 mg/ml. Fifty microliters of purified CAF-1 or CAF-1–H3-H4 complexes in the presence and absence of DNA$_{30}$ at a concentration of ~1 mg/ml each were subjected to the system at a flow rate of 0.5 ml/min at room temperature. Data were analyzed by the ASTRA software.

Single-molecule FOMT analysis

A multiple digoxigenin-labeled and multiple biotin-labeled 159-bp DNA segment was amplified by PCR and ligated with handle DNA (543 bp) via the *Sty*I restriction site. Purified ligation products were further ligated with the 147-bp Widom 601 DNA via the *Bsa*I restriction site, and the full-ligation product was purified by gel extraction.

Upon treating the coverslips with piranha solution, polystyrene beads (2 µm, QDSpher) were loaded and incubated at 150°C for 8 min on a hot plate, and the beads served as the reference to control thermal drifts during the experiment. Then, the coverslips were coated with Sigmacote (Sigma-Aldrich, SL2) for 5 min and the flow-cells were incubated with 100 µl of antidigoxigenin (0.1 mg/ml, Roche) in PBS for 4 hours at 4°C. This was followed by passivation of the flow-cell with 100 µl of passivation buffer [10 mg/ml BSA, 1 mM EDTA, 10 mM phosphate buffer, pH 8.0, 10 mg/ml Pluronic F127 surfactant (Sigma-Aldrich, P2443), and 3 mM NaN$_3$] at 4°C overnight.

FOMTs (*54*, *82*), as schematically shown in Fig. 6D, were built based on homemade single-molecule magnetic tweezers described before (*83*). Force calibration was carried out by tethering an 8-kb DNA between the superparamagnetic bead (Dynabeads MyOne Streptavidin T1, Invitrogen, 65601) and the coverslip, following published procedures (*82*, *84*), with the recording of freely rotating magnetic beads positioned under a force ranging from 0.45 to 1.8 pN.

After the flow-cell was rinsed with 1 ml of FOMT buffer (50 mM KCl, 25 mM HEPES, pH 7.5, 0.1 mM EDTA, 0.025% PEG, 0.025% PVOH, and 1 mg/ml BSA), 100 µl of purified full-ligated DNA (3 pg/µl) in FOMT buffer was loaded and incubated at room temperature for 20 min before the flow-cell was further washed with 200 µl of FOMT buffer. Superparamagnetic bead (T1) in FOMT buffer was added to the flow-cell and incubated for 20 min at room temperature. Then, 200 µl of FOMT buffer was flowed into the flow-cell to flush away the unbounded beads.

Yeast Nap1-H3H4 (200 nM) and human CAF1-FC–H3-H4 (50 nM) complexes were kept in the preincubation buffer (50 mM KCl, 25 mM HEPES, pH 7.5, 0.1 mM EDTA, 0.25% PEG, 0.25% PVOH, and 1 mg/ml BSA) at 4°C for 30 min. Then the complexes were loaded into the flow-cell with 100 times dilution. The bead image was captured by a JAI Giga-Ethernet CCD camera at 500 Hz for 4 hours through the inverted microscope objective lens (UPLXAPO60XO, NA 1.42, Olympus). The real-time position (x, y, z) of the beads at 0.7 pN was recorded with the comparison between the diffraction pattern of the beads and calibration images at various distances from the focal point of the objective.

The circle center (x_c, y_c) and radius R_{circle} of the beads' trajectories are fitted using the least squares method, that is, minimizing the sum of the squares of the residuals:

$$\min_{x_c, y_c, R_{circle}} = \sum_i \left[(x_i - x_c)^2 + (y_i - y_c)^2 - R_{circle}{}^2 \right] \quad (1)$$

To calculate parameters x_c, y_c, and R_{circle} from the bead's position (x_i, y_i), we defined matrix A and vector $\vec{b}, \vec{x}$:

$$A = \begin{pmatrix} x_1 & y_1 & 1 \\ x_1 & y_2 & 1 \\ \cdots & \cdots & \cdots \\ x_n & y_n & 1 \end{pmatrix},$$

$$\vec{b} = \begin{pmatrix} x_1{}^2 + y_1{}^2 \\ x_2{}^2 + y_2{}^2 \\ \cdots \\ x_n{}^2 + y_n{}^2 \end{pmatrix}, \text{and}$$

$$\vec{x} = \begin{pmatrix} 2x_c \\ 2y_c \\ r^2 - x_c{}^2 - y_c{}^2 \end{pmatrix} \quad (2)$$

The overdetermined system is

$$A\vec{x} = \vec{b} \quad (3)$$

The solution of which is given by

$$\vec{x} = \left(A^{\mathrm{T}} A \right)^{-1} A^{\mathrm{T}} \vec{b} \quad (4)$$

After finding x_c, y_c, and R_{circle}, we set the pole of the polar coordinates system as (x_c, y_c). By denoting the bead's position vector (x_i, y_i) as $\vec{r}_i$, the rotation from position $\vec{r}_i$ to $\vec{r}_{i+1}$ is given by

$$\Delta\theta_{i,i+1} = \arccos \frac{\langle \vec{r}_i, \vec{r}_{i+1} \rangle}{|\vec{r}_i||\vec{r}_{i+1}|} \quad (5)$$

The angles of rotation from the initial position are given by

$$\theta_k = \begin{cases} \sum_{i=1}^{k-1} \Delta\theta_{i,i+1}, & \Delta\theta_{i,i+1} \\ 0, & k = 1 \end{cases} \quad (6)$$

The polar coordinates (r_i, ϕ_i) are given by

$$r_i = \sqrt{(x_i - x_c)^2 + (y_i - y_c)^2} \qquad (7)$$

$$\phi_i = \arctan\left(\frac{y_i - y_c}{x_i - x_c}\right) \qquad (8)$$

The code used for analyzing and plotting FOMT data is archived at Zenodo (*85*).

EMSA

In each EMSA reaction (total volume of 20 μl), a mixture of 0.5 μM 147-bp DNA with 0.5, 1, 2.5, 5, or 10 μM of p60ΔC or p48, in a buffer containing 20 mM Tris-HCl, pH 7.5, 50 mM NaCl, and 1 mM DTT, was first incubated on ice for 30 min, followed by electrophoresis on a 6% native polyacrylamide gel at 120 V for 50 min with 0.5× TBE buffer in an ice-water bath. The gel was stained by SYBR Gold (Thermo Fisher) and visualized with the Gel Doc EZ imaging System (Bio-Rad).

Quantification and statistical analysis

The orientation distribution of the particles used in the final reconstructions and the local resolution maps were calculated using cryoSPARC (*68*). The quantification and statistical analyses for model refinement and validation were generated using MolProbity (*64*). Data for cell proliferation assays are from three biological replicates, and a two-way analysis of variance (ANOVA) with Šídák test was used to calculate *p* values. Data for RNA-seq are presented with two biological replicates.

REFERENCES AND NOTES

1. K. Luger, A. W. Mäder, R. K. Richmond, D. F. Sargent, T. J. Richmond, Crystal structure of the nucleosome core particle at 2.8 A resolution. *Nature* **389**, 251–260 (1997). doi: 10.1038/38444; pmid: 9305837
2. A. Serra-Cardona, Z. Zhang, Replication-coupled nucleosome assembly in the passage of epigenetic information and cell identity. *Trends Biochem. Sci.* **43**, 136–148 (2018). doi: 10.1016/j.tibs.2017.12.003; pmid: 29292063
3. A. Groth, W. Rocha, A. Verreault, G. Almouzni, Chromatin challenges during DNA replication and repair. *Cell* **128**, 721–733 (2007). doi: 10.1016/j.cell.2007.01.030; pmid: 17320509
4. M. Xu *et al.*, Partitioning of histone H3-H4 tetramers during DNA replication-dependent chromatin assembly. *Science* **328**, 94–98 (2010). doi: 10.1126/science.1178994; pmid: 20360108
5. C. Yu *et al.*, A mechanism for preventing asymmetric histone segregation onto replicating DNA strands. *Science* **361**, 1386–1389 (2018). doi: 10.1126/science.aat8849; pmid: 30115745
6. N. Petryk *et al.*, MCM2 promotes symmetric inheritance of modified histones during DNA replication. *Science* **361**, 1389–1392 (2018). doi: 10.1126/science.aau0294; pmid: 30115746
7. S. Smith, B. Stillman, Purification and characterization of CAF-I, a human cell factor required for chromatin assembly during DNA replication in vitro. *Cell* **58**, 15–25 (1989). doi: 10.1016/0092-8674(89)90398-X; pmid: 2546672
8. S. Smith, B. Stillman, Stepwise assembly of chromatin during DNA replication in vitro. *EMBO J.* **10**, 971–980 (1991). doi: 10.1002/j.1460-2075.1991.tb08031.x; pmid: 1849080
9. P. D. Kaufman, R. Kobayashi, N. Kessler, B. Stillman, The p150 and p60 subunits of chromatin assembly factor I: A molecular link between newly synthesized histones and DNA replication. *Cell* **81**, 1105–1114 (1995). doi: 10.1016/S0092-8674(05)80015-7; pmid: 7600578
10. Z. Zhang, B. Shibahara, B. Stillman, PCNA connects DNA replication to epigenetic inheritance in yeast. *Nature* **408**, 221–225 (2000). doi: 10.1038/35041601; pmid: 11089978
11. K. Shibahara, B. Stillman, Replication-dependent marking of DNA by PCNA facilitates CAF-1-coupled inheritance of chromatin. *Cell* **96**, 575–585 (1999). doi: 10.1016/S0092-8674(00)80661-3; pmid: 10052459
12. J. K. Tyler *et al.*, The RCAF complex mediates chromatin assembly during DNA replication and repair. *Nature* **402**, 555–560 (1999). doi: 10.1038/990147; pmid: 10591219
13. J. A. Sharp, E. T. Fouts, D. C. Krawitz, P. D. Kaufman, Yeast histone deposition protein Asf1p requires Hir proteins and PCNA for heterochromatic silencing. *Curr. Biol.* **11**, 463–473 (2001). doi: 10.1016/S0960-9822(01)00140-3; pmid: 11412995
14. M. Hoek, B. Stillman, Chromatin assembly factor 1 is essential and couples chromatin assembly to DNA replication in vivo. *Proc. Natl. Acad. Sci. U.S.A.* **100**, 12183–12188 (2003). doi: 10.1073/pnas.1635158100; pmid: 14519857
15. S. Enomoto, P. D. McCune-Zierath, M. Gerami-Nejad, M. A. Sanders, J. Berman, RLF2, a subunit of yeast chromatin assembly factor-I, is required for telomeric chromatin function in vivo. *Genes Dev.* **11**, 358–370 (1997). doi: 10.1101/gad.11.3.358; pmid: 9030688
16. P. D. Kaufman, R. Kobayashi, B. Stillman, Ultraviolet radiation sensitivity and reduction of telomeric silencing in *Saccharomyces cerevisiae* cells lacking chromatin assembly factor-I. *Genes Dev.* **11**, 345–357 (1997). doi: 10.1101/gad.11.3.345; pmid: 9030687
17. Q. Li *et al.*, Acetylation of histone H3 lysine 56 regulates replication-coupled nucleosome assembly. *Cell* **134**, 244–255 (2008). doi: 10.1016/j.cell.2008.06.018; pmid: 18662540
18. H. Tagami, D. Ray-Gallet, G. Almouzni, Y. Nakatani, Histone H3.1 and H3.3 complexes mediate nucleosome assembly pathways dependent or independent of DNA synthesis. *Cell* **116**, 51–61 (2004). doi: 10.1016/S0092-8674(03)01064-X; pmid: 14718166
19. K. Ahmad, S. Henikoff, The histone variant H3.3 marks active chromatin by replication-independent nucleosome assembly. *Mol. Cell* **9**, 1191–1200 (2002). doi: 10.1016/S1097-2765(02)00542-7; pmid: 12086617
20. E. Martini, D. M. Roche, K. Marheineke, A. Verreault, G. Almouzni, Recruitment of phosphorylated chromatin assembly factor 1 to chromatin after UV irradiation of human cells. *J. Cell Biol.* **143**, 563–575 (1998). doi: 10.1083/jcb.143.3.563; pmid: 9813080
21. P. Ridgway, G. Almouzni, CAF-1 and the inheritance of chromatin states: At the crossroads of DNA replication and repair. *J. Cell Sci.* **113**, 2647–2658 (2000). doi: 10.1242/jcs.113.15.2647; pmid: 10893180
22. S. Cheloufi, K. Hochedlinger, Emerging roles of the histone chaperone CAF-1 in cellular plasticity. *Curr. Opin. Genet. Dev.* **46**, 83–94 (2017). doi: 10.1016/j.gde.2017.06.004; pmid: 28692904
23. A. Verreault, P. D. Kaufman, R. Kobayashi, B. Stillman, Nucleosome assembly by a complex of CAF-1 and acetylated histones H3/H4. *Cell* **87**, 95–104 (1996). doi: 10.1016/S0092-8674(00)81326-4; pmid: 8858152
24. P. V. Sauer *et al.*, Mechanistic insights into histone deposition and nucleosome assembly by the chromatin assembly factor-1. *Nucleic Acids Res.* **46**, 9907–9917 (2018). doi: 10.1093/nar/gky823; pmid: 30239791
25. T. Rolef Ben-Shahar *et al.*, Two fundamentally distinct PCNA interaction peptides contribute to chromatin assembly factor 1 function. *Mol. Cell. Biol.* **29**, 6353–6365 (2009). doi: 10.1128/MCB.01051-09; pmid: 19822659
26. A. Volk, J. D. Crispino, The role of the chromatin assembly complex (CAF-1) and its p60 subunit (CHAF1b) in homeostasis and disease. *Biochim. Biophys. Acta* **1849**, 979–986 (2015). doi: 10.1016/j.bbagrm.2015.05.009; pmid: 26066981
27. S. E. Polo *et al.*, Chromatin assembly factor-1, a marker of clinical value to distinguish quiescent from proliferating cells. *Cancer Res.* **64**, 2371–2381 (2004). doi: 10.1158/0008-5472.CAN-03-2893; pmid: 15059888
28. K. S. Shim *et al.*, Reduction of chromatin assembly factor 1 p60 and C21orf2 protein, encoded on chromosome 21, in Down syndrome brain. *J. Neural Transm. Suppl.* **67**, 117–128 (2003). doi: 10.1007/978-3-7091-6721-2_10; pmid: 15068244
29. Y. Tang *et al.*, Structure of a human ASF1a-HIRA complex and insights into specificity of histone chaperone complex assembly. *Nat. Struct. Mol. Biol.* **13**, 921–929 (2006). doi: 10.1038/nsmb1147; pmid: 16980972
30. F. Mattiroli, Y. Gu, J. L. Balsbaugh, N. G. Ahn, K. Luger, The Cac2 subunit is essential for productive histone binding and nucleosome assembly in CAF-1. *Sci. Rep.* **7**, 46274 (2017). doi: 10.1038/srep46274; pmid: 28418026
31. J. K. Tyler, M. Bulger, R. T. Kamakaka, R. Kobayashi, J. T. Kadonaga, The p55 subunit of *Drosophila* chromatin assembly factor 1 is homologous to a histone deacetylase-associated protein. *Mol. Cell. Biol.* **16**, 6149–6159 (1996). doi: 10.1128/MCB.16.11.6149; pmid: 8887645
32. A. Verreault, P. D. Kaufman, R. Kobayashi, B. Stillman, Nucleosomal DNA regulates the core-histone-binding subunit of the human Hat1 acetyltransferase. *Curr. Biol.* **8**, 96–108 (1998). doi: 10.1016/S0960-9822(98)70040-5; pmid: 9427644
33. Y. Yue, W. S. Yang, L. Zhang, C. P. Liu, R. M. Xu, Topography of histone H3-H4 interaction with the Hat1-Hat2 acetyltransferase complex. *Genes Dev.* **36**, 408–413 (2022). doi: 10.1101/gad.349099.121; pmid: 35393344
34. D. Kim *et al.*, Molecular architecture of yeast Chromatin Assembly Factor 1. *Sci. Rep.* **6**, 26702 (2016). doi: 10.1038/srep26702; pmid: 27221973
35. P. V. Sauer *et al.*, Insights into the molecular architecture and histone H3-H4 deposition mechanism of yeast Chromatin assembly factor 1. *eLife* **6**, e23474 (2017). doi: 10.7554/eLife.23474; pmid: 28315525
36. K. Zhang *et al.*, A DNA binding winged helix domain in CAF-1 functions with PCNA to stabilize CAF-1 at replication forks. *Nucleic Acids Res.* **44**, 5083–5094 (2016). doi: 10.1093/nar/gkw106; pmid: 26908650
37. H. Wang, M. Wang, N. Yang, R. M. Xu, Structure of the quaternary complex of histone H3-H4 heterodimer with chaperone ASF1 and the replicative helicase subunit MCM2. *Protein Cell* **6**, 693–697 (2015). doi: 10.1007/s13238-015-0190-0; pmid: 26186914
38. N. Richet *et al.*, Structural insight into how the human helicase subunit MCM2 may act as a histone chaperone together with ASF1 at the replication fork. *Nucleic Acids Res.* **43**, 1905–1917 (2015). doi: 10.1093/nar/gkv021; pmid: 25618846
39. H. Huang *et al.*, A unique binding mode enables MCM2 to chaperone histones H3-H4 at replication forks. *Nat. Struct. Mol. Biol.* **22**, 618–626 (2015). doi: 10.1038/nsmb.3055; pmid: 26167883
40. A. Groth *et al.*, Regulation of replication fork progression through histone supply and demand. *Science* **318**, 1928–1931 (2007). doi: 10.1126/science.1148992; pmid: 18096887
41. X. Ye *et al.*, Defective S phase chromatin assembly causes DNA damage, activation of the S phase checkpoint, and S phase arrest. *Mol. Cell* **11**, 341–351 (2003). doi: 10.1016/S1097-2765(03)00037-6; pmid: 12620223
42. S. Ramachandran, S. Henikoff, MINCE-Seq: Mapping in vivo nascent chromatin with EdU and sequencing. *Methods Mol. Biol.* **1832**, 159–168 (2018). doi: 10.1007/978-1-4939-8663-7_8; pmid: 30073526
43. Z. Xu, J. Feng, Q. Li, Measuring genome-wide nascent nucleosome assembly using ReIN-Map. *Methods Mol. Biol.* **2196**, 117–141 (2021). doi: 10.1007/978-1-0716-0868-5_10; pmid: 32889717
44. A. Yesbolatova *et al.*, The auxin-inducible degron 2 technology provides sharp degradation control in yeast, mammalian cells, and mice. *Nat. Commun.* **11**, 5701 (2020). doi: 10.1038/s41467-020-19532-z; pmid: 33177522
45. E. K. Monson, D. de Bruin, V. A. Zakian, The yeast Cac1 protein is required for the stable inheritance of transcriptionally repressed chromatin at telomeres. *Proc. Natl. Acad. Sci. U.S.A.* **94**, 13081–13086 (1997). doi: 10.1073/pnas.94.24.13081; pmid: 9371803
46. F. Tessadori *et al.*, Recurrent de novo missense variants across multiple histone H4 genes underlie a neurodevelopmental syndrome. *Am. J. Hum. Genet.* **109**, 750–758 (2022). doi: 10.1016/j.ajhg.2022.02.003; pmid: 35202563
47. S. Cheloufi *et al.*, The histone chaperone CAF-1 safeguards somatic cell identity. *Nature* **528**, 218–224 (2015). doi: 10.1038/nature15749; pmid: 26659182
48. R. Franklin *et al.*, Regulation of chromatin accessibility by the histone chaperone CAF-1 sustains lineage fidelity. *Nat. Commun.* **13**, 2350 (2022). doi: 10.1038/s41467-022-29730-6; pmid: 35487911
49. T. Ishiuchi *et al.*, Early embryonic-like cells are induced by downregulating replication-dependent chromatin assembly. *Nat. Struct. Mol. Biol.* **22**, 662–671 (2015). doi: 10.1038/nsmb.3066; pmid: 26237512
50. L. Cheng *et al.*, Chromatin Assembly Factor 1 (CAF-1) facilitates the establishment of facultative heterochromatin during pluripotency exit. *Nucleic Acids Res.* **47**, 11114–11131 (2019). doi: 10.1093/nar/gkz858; pmid: 31586391
51. C. M. Hammond, C. B. Strømme, H. Huang, D. J. Patel, A. Groth, Histone chaperone networks shaping chromatin function. *Nat. Rev. Mol. Cell Biol.* **18**, 141–158 (2017). doi: 10.1038/nrm.2016.159; pmid: 28053344
52. F. Mattiroli *et al.*, DNA-mediated association of two histone-bound complexes of yeast Chromatin Assembly Factor-1 (CAF-1) drives

tetrasome assembly in the wake of DNA replication. *eLife* **6**, e22799 (2017). doi: 10.7554/eLife.22799; pmid: 28315523

53. K. Nozawa *et al.*, Cryo-electron microscopy structure of the H3-H4 octasome: A nucleosome-like particle without histones H2A and H2B. *Proc. Natl. Acad. Sci. U.S.A.* **119**, e2206542119 (2022). doi: 10.1073/pnas.2206542119; pmid: 36322721

54. R. Vlijm *et al.*, Nucleosome assembly dynamics involve spontaneous fluctuations in the handedness of tetrasomes. *Cell Rep.* **10**, 216–225 (2015). doi: 10.1016/j.celrep.2014.12.022; pmid: 25578730

55. C. Rouillon *et al.*, CAF-1 deposits newly synthesized histones during DNA replication using distinct mechanisms on the leading and lagging strands. *Nucleic Acids Res.* **51**, 3770–3792 (2023). doi: 10.1093/nar/gkad171; pmid: 36942484

56. J. Fei *et al.*, The prenucleosome, a stable conformational isomer of the nucleosome. *Genes Dev.* **29**, 2563–2575 (2015). doi: 10.1101/gad.272633.115; pmid: 26680301

57. A. Hamiche *et al.*, Interaction of the histone (H3-H4)2 tetramer of the nucleosome with positively supercoiled DNA minicircles: Potential flipping of the protein from a left- to a right-handed superhelical form. *Proc. Natl. Acad. Sci. U.S.A.* **93**, 7588–7593 (1996). doi: 10.1073/pnas.93.15.7588; pmid: 8755519

58. T. Furuyama, S. Henikoff, Centromeric nucleosomes induce positive DNA supercoils. *Cell* **138**, 104–113 (2009). doi: 10.1016/j.cell.2009.04.049; pmid: 19596238

59. X. Ming *et al.*, Kinetics and mechanisms of mitotic inheritance of DNA methylation and their roles in aging-associated methylome deterioration. *Cell Res.* **30**, 980–996 (2020). doi: 10.1038/s41422-020-0359-9; pmid: 32581343

60. Z. Otwinowski, W. Minor, Processing of X-ray diffraction data collected in oscillation mode. *Methods Enzymol.* **276**, 307–326 (1997). doi: 10.1016/S0076-6879(97)76066-X; pmid: 27754618

61. A. J. McCoy *et al.*, Phaser crystallographic software. *J. Appl. Crystallogr.* **40**, 658–674 (2007). doi: 10.1107/S0021889807021206; pmid: 19461840

62. P. Emsley, K. Cowtan, Coot: Model-building tools for molecular graphics. *Acta Crystallogr. D Biol. Crystallogr.* **60**, 2126–2132 (2004). doi: 10.1107/S0907444904019158; pmid: 15572765

63. P. D. Adams *et al.*, PHENIX: A comprehensive Python-based system for macromolecular structure solution. *Acta Crystallogr. D Biol. Crystallogr.* **66**, 213–221 (2010). doi: 10.1107/S0907444909052925; pmid: 20124702

64. V. B. Chen *et al.*, MolProbity: All-atom structure validation for macromolecular crystallography. *Acta Crystallogr. D Biol. Crystallogr.* **66**, 12–21 (2010). doi: 10.1107/S0907444909042073; pmid: 20057044

65. P. N. Dyer *et al.*, Reconstitution of nucleosome core particles from recombinant histones and DNA. *Methods Enzymol.* **375**, 23–44 (2004). doi: 10.1016/S0076-6879(03)75002-2; pmid: 14870657

66. P. T. Lowary, J. Widom, New DNA sequence rules for high affinity binding to histone octamer and sequence-directed nucleosome positioning. *J. Mol. Biol.* **276**, 19–42 (1998). doi: 10.1006/jmbi.1997.1494; pmid: 9514715

67. B. Kastner *et al.*, GraFix: Sample preparation for single-particle electron cryomicroscopy. *Nat. Methods* **5**, 53–55 (2008). doi: 10.1038/nmeth1139; pmid: 18157137

68. A. Punjani, J. L. Rubinstein, D. J. Fleet, M. A. Brubaker, cryoSPARC: Algorithms for rapid unsupervised cryo-EM structure determination. *Nat. Methods* **14**, 290–296 (2017). doi: 10.1038/nmeth.4169; pmid: 28165473

69. K. Zhang, Gctf: Real-time CTF determination and correction. *J. Struct. Biol.* **193**, 1–12 (2016). doi: 10.1016/j.jsb.2015.11.003; pmid: 26592709

70. J. Zivanov *et al.*, New tools for automated high-resolution cryo-EM structure determination in RELION-3. *eLife* **7**, e42166 (2018). doi: 10.7554/eLife.42166; pmid: 30412051

71. D. Asarnow, E. Palovcak, Y. Cheng, UCSF pyem v0.5. *Zenodo* (2019). doi: 10.5281/zenodo.3576630

72. E. F. Pettersen *et al.*, UCSF Chimera—A visualization system for exploratory research and analysis. *J. Comput. Chem.* **25**, 1605–1612 (2004). doi: 10.1002/jcc.20084; pmid: 15264254

73. T. D. Goddard *et al.*, UCSF ChimeraX: Meeting modern challenges in visualization and analysis. *Protein Sci.* **27**, 14–25 (2018). doi: 10.1002/pro.3235; pmid: 28710774

74. A. Osakabe *et al.*, Nucleosome formation activity of human somatic nuclear autoantigenic sperm protein (sNASP). *J. Biol. Chem.* **285**, 11913–11921 (2010). doi: 10.1074/jbc.M109.083238; pmid: 20167597

75. J. Xiong *et al.*, Cooperative action between SALL4A and TET proteins in stepwise oxidation of 5-methylcytosine. *Mol. Cell* **64**, 913–925 (2016). doi: 10.1016/j.molcel.2016.10.013; pmid: 27840027

76. S. Ramachandran, S. Henikoff, Transcriptional regulators compete with nucleosomes post-replication. *Cell* **165**, 580–592 (2016). doi: 10.1016/j.cell.2016.02.062; pmid: 27062929

77. S. Liu *et al.*, RPA binds histone H3-H4 and functions in DNA replication-coupled nucleosome assembly. *Science* **355**, 415–420 (2017). doi: 10.1126/science.aah4712; pmid: 28126821

78. J. Yu *et al.*, Analysis of local chromatin states reveals gene transcription potential during mouse neural progenitor cell differentiation. *Cell Rep.* **32**, 107953 (2020). doi: 10.1016/j.celrep.2020.107953; pmid: 32726618

79. B. Langmead, S. L. Salzberg, Fast gapped-read alignment with Bowtie 2. *Nat. Methods* **9**, 357–359 (2012). doi: 10.1038/nmeth.1923; pmid: 22388286

80. K. Chen *et al.*, DANPOS: Dynamic analysis of nucleosome position and occupancy by sequencing. *Genome Res.* **23**, 341–351 (2013). doi: 10.1101/gr.142067.112; pmid: 23193179

81. J. H. I. Haarhuis *et al.*, A Mediator-cohesin axis controls heterochromatin domain formation. *Nat. Commun.* **13**, 754 (2022). doi: 10.1038/s41467-022-28377-7; pmid: 35136067

82. J. Lipfert, M. Wiggin, J. W. Kerssemakers, F. Pedaci, N. H. Dekker, Freely orbiting magnetic tweezers to directly monitor changes in the twist of nucleic acids. *Nat. Commun.* **2**, 439 (2011). doi: 10.1038/ncomms1450; pmid: 21863006

83. P. Chen *et al.*, Functions of FACT in breaking the nucleosome and maintaining its integrity at the single-nucleosome level. *Mol. Cell* **71**, 284–293.e4 (2018). doi: 10.1016/j.molcel.2018.06.020; pmid: 30029006

84. A. J. te Velthuis, J. W. Kerssemakers, J. Lipfert, N. H. Dekker, Quantitative guidelines for force calibration through spectral analysis of magnetic tweezers data. *Biophys. J.* **99**, 1292–1302 (2010). doi: 10.1016/j.bpj.2010.06.008; pmid: 20713015

85. Z. Li, Code for analysis and plotting data from freely orbiting magnetic tweezers (1.0). *Zenodo* (2023); https://doi.org/10.5281/zenodo.8166291.

ACKNOWLEDGMENTS

SUPPLEMENTARY MATERIALS